

Electrons from heavy-flavor semileptonic decays in proton-proton collisions at $\sqrt{s}=13$ TeV measured with the ALICE detector at the LHC

Master's thesis by Madeleine Petersson Sjögren
Supervised by David Silvermyr

Lund University
Division of Particle Physics
Department of Physics

February 1, 2018



LUND
UNIVERSITY

Abstract

Heavy-flavor hadrons, containing charm and bottom quarks, serve as a tool available for the characterization of the hot and dense strongly interacting Quark Gluon Plasma state of matter, produced in heavy-ion collisions. As a benchmark for heavy-ion collision measurements, proton-proton collisions are also studied. This thesis reports on the analysis of proton-proton collisions, reconstructed with the ALICE detector at $\sqrt{s} = 13$ TeV, to measure heavy-flavor semileptonic decays to electrons, for $2 < p_T < 10$ GeV/ c . The project described here employs two different methods for the description of number of electrons from heavy-flavor hadrons, where the first analysis makes use of a background estimation and photon-electron rejection from the heavy-flavor electron candidates sample. The second analysis employs measurements of the fraction of electrons from heavy-flavor hadrons, as compared to other sources, by study of the Distance of Closest approach (DCA) distributions of particle tracks. The methods used are described and the results are presented and discussed together with an outlook for this project.

Acknowledgements

I would like to thank David Silvermyr and Peter Christiansen for introducing me to the study on QGP and for all their support, help and feedback during the whole project. Many thanks to Anders Oskarsson, Evert Stenlund, Tuva Richert, Vytautas Vislavicius, Jonatan Adolfsson and Martin Ljunggren for sharing their invaluable expertise on both particle physics and programming throughout the passed year and also for their feedback on this report. Also, great thanks to Maria Mårtenson, Adam Johansson, Adrian Nassirpour and Rickard Lydahl for fruitful discussions and a lot of fun during this process.

Populärvetenskaplig sammanfattning

Partikelfysik, också kallat högenergifysik, är studiet av de minsta partiklarna: elementarpartiklarna och deras växelverkan med varandra. Genom att accelerera partiklar till höga energier och låta dem kollidera, med ett fixerat mål eller en annan skur av partiklar, skapas tillstånd och partiklar som vanligtvis inte förekommer i vår värld. Partikelfysikforskning bedrivs i huvudsak genom att studera partiklarna som kommer ut ur partikelkollisioner.

Med tungjonskollisioner har man funnit att ett alldeles särskilt tillstånd av materia skapas: ett så kallat Kvarck Gluon Plasma (QGP). Detta tillstånd är unikt på så sätt att kvarkar och gluoner, som vanligtvis alltid är bundna i större sammansatta partiklar benämnda hadroner, beter sig i Kvarck Gluon Plasmat som om de vore nästan helt fria. Kvarck Gluon Plasma tillverkas idag i kollisioner av bly-kärnor vid the Large Hadron Collider (LHC) på CERN (European Organization of Nuclear Research). Kvarck Gluon Plasmat är extremt kortlivat, med en livstid på omkring ett par fm/c ($\sim 10^{-23}$ sekunder), vilket omöjliggör direkta studier och undersökningar av QGP:n. För att karakterisera och undersöka QGP:ns egenskaper måste man istället studera partiklarna och tillstånden som kommer ut från partikelkollisionerna.

I huvudsak vill man via studiet av Kvarck Gluon Plasmat karakterisera signaler som indikerar att ett Kvarck Gluon Plasma tillverkats och hur Kvarck Gluon Plasmat utvecklar sig rumsligt. En sådan metod involverar de tunga kvarkarna, *charm* och *botten*. Dessa kvarkar skapas tidigt i partikelkollisioner, innan bildandet av ett Kvarck Gluon Plasma, varpå de kan röra sig genom det unika mediumet. Genom analyser av hur de tunga kvarkarna beter sig i Kvarck Gluon Plasmat kan man dra slutsatser om plasmats egenskaper, så som densitet och temperatur.

För att studera tunga kortlivade partiklar, så som hadroner som består av tunga kvarkar, studeras partiklarnas sönderfallsprodukter. Ofta refererar man till partikeln som sönderfaller som *moderpartikeln* medan sönderfallsprodukterna är dess *dotter-partiklar*. I denna rapport beskrivs en dataanalys av proton-proton kollisioner i LHC detekterade med ALICE (A Large Ion Collider Experiment) -detektorn. Dataanalysen är konstuerad för att bestämma antalet elektroner från tunga-kvark partiklars sönderfall. Motiveringen bakom analysen av proton-proton, kollisioner istället för studiet av tunga-kärn-kollisioner eller kollisioner av kärnor med protoner, är att det för analysen av kärn-kollisioner behövs proton-proton-kollision analyser som referens.

List of acronyms

- ALICE A Large Ion Collider Experiment
- CERN European Organization of Nuclear Research
- EMCal Electromagnetic Calorimeter
- ITS Inner Tracking System
- LHC Large Hadron Collider
- MC Monte Carlo
- MWPC Multi-Wire Proportional Chamber
- NN Nucleon-Nucleon
- PbPb lead-lead
- pp proton-proton
- pA proton-nucleus
- pPb proton-lead
- PID Particle Identification
- QCD Quantum Chromodynamics
- QGP Quark Gluon Plasma
- SPD Silicon Pixel Detector
- TPC Time Projection Chamber

Contents

1	Introduction and aim	1
2	Theoretical overview	2
2.1	The Standard Model	2
2.1.1	Fermions: quarks and leptons	3
2.1.2	Gauge bosons and the fundamental forces	4
2.1.3	Quantum Chromodynamics	4
2.1.4	Strongly interacting matter	7
3	Experimental particle physics	8
3.1	Definitions	9
3.1.1	Transverse momentum	9
3.1.2	Center-of-mass energy	9
3.1.3	Rapidity and Pseudorapidity	10
3.1.4	Impact parameter, centrality and multiplicity	10
3.1.5	Invariant mass	10
3.2	Heavy-ion collisions	11
3.2.1	A de-confined state of matter	12
3.2.2	QGP signals	13
3.2.3	Heavy-flavor as a signal of QGP	15
4	The ALICE experiment at the LHC	17
4.1	The ALICE experiment	18
4.1.1	The Time Projection Chamber (TPC)	20
4.1.2	The Electromagnetic Calorimeter (EMCal)	21
5	Method of Analysis	23
5.1	Data, software used and event selection	23
5.2	Electron mother-particle analysis	24
5.3	Track selection	26
5.4	Electron identification	26
5.5	Non-electron background subtraction	29
5.6	Photon electron rejection	30
5.7	Detector efficiency	34
5.8	Electron mother DCA distribution analysis	38
6	Results and discussion	42
6.1	Electron yield from spectra analysis	42
6.2	DCA _{xy} distribution fractional yields	44
6.3	Conclusion and outlook	47
7	Appendix	

1 Introduction and aim

Particle physics research is the study of fundamental constituents of matter and how these building blocks interact with each other, making the world look and behave the way it does. Such research incorporates theoretical investigations on how things should behave, based on mathematical models, combined with high energy experiments.

Today's largest particle physics experiments make use of huge particle accelerators, where composite particles, such as protons and nuclei, are accelerated to high energy before they are set to collide. The available energy within the collision enables the production of particles and states of matter that were not there from the beginning. Quantum Chromodynamics (QCD) is the theory which describes the strong interaction between quarks, the building blocks of matter, and gluons, the carriers of the strong interaction. Analyses of particle collisions provides tests of the QCD theory through the characterization of the behavior of strongly interacting matter in a high temperature and high density regime, created in the collisions. Under such conditions, QCD predicts the existence of a de-confined medium called the Quark Gluon Plasma (QGP).

Heavy-flavor particles, such as charm- and bottom-quarks, are dominantly produced in initial hard parton scattering processes, presumably before the formation of a QGP. Consequently, these particles can probe the hot and dense QGP state of matter, as they traverse it. Color-charge and mass dependence of particle energy loss is studied by comparing suppressions of the heavy-flavor hadron yield with hadrons carrying only lighter quarks, such as up and down quarks. Heavy-flavor production measurements in proton-proton (pp) collisions provide a baseline for corresponding analyses in nucleus-nucleus (AA) and proton-nucleus (pA) collisions.

This thesis reports on the mid rapidity ($|\eta| < 0.6$) production of electrons from semileptonic heavy-flavor hadron decays measured with the ALICE [1] detector at the Large Hadron Collider (LHC) in the range $2 \leq p_T \leq 10$ GeV/ c in pp collisions at $\sqrt{s_{NN}} = 13$ TeV. Electron candidates were selected using the Time Projection Chamber (TPC) [2] and the Electromagnetic Calorimeter (EMCal) [3]. Two independent techniques have been employed to study electrons from heavy-flavor. The first analysis consists of studies of the contribution of semileptonic decays from heavy-flavor hadrons to the electron spectra and the other using the Distance of Closest Approach (DCA) distributions of electrons, in order to try to distinguish the fraction of electrons from heavy-flavor, from other sources. The analysis techniques used are very much inspired by [4], [5] and [6]. The first analysis consists of the following steps: electron particle identification, non-electron background estimation, photon rejection and efficiency correction. The second analysis presented here consists of the same electron identification and photon rejection as in the first part, followed by a study of the electron DCA_{xy} distributions incorporating the use of MC data simulations.

2 Theoretical overview

2.1 The Standard Model

Modern-physics research describes phenomena from the small scale of quarks and leptons ($< 10^{-18}$ m) to the scale of solar systems and galaxies, by the concept of four fundamental interactions: electromagnetism, strong interaction, weak interaction and gravity. The current understanding of the interactions, or forces, are described by the Standard Model (SM) of particle physics, in which interactions between elementary particles are described by the exchange of other particles. All the three first-mentioned interactions are described by the SM, while gravity is described by Einstein's theory of general relativity. The SM is a quantum field theory of elementary particles, and it is consistent with Einstein's special theory of relativity, and quantum mechanics. SM is a triumph of modern physics and has so far been successful in describing almost all experimental data [7].

Within the SM, all elementary particles are categorized into two subgroups, *fermions* and *bosons*, depending on their spin. All spin 1/2 particles are fermions of the type leptons or quarks, and these are the building blocks of matter. All integer spin particles are bosons. Currently, there are five known bosons of the SM. These are the four gauge bosons with spin 1, which are mediators of the forces, and one scalar boson with spin 0, the Higgs boson, described by the Higgs mechanism, which will not be further mentioned here.

Figure 1 shows the particles of the Standard Model divided into quarks (in purple), leptons (in green) and bosons in red and yellow. There are in total twelve fermions, six quarks and six leptons, four gauge bosons and one scalar boson, the Higgs boson.

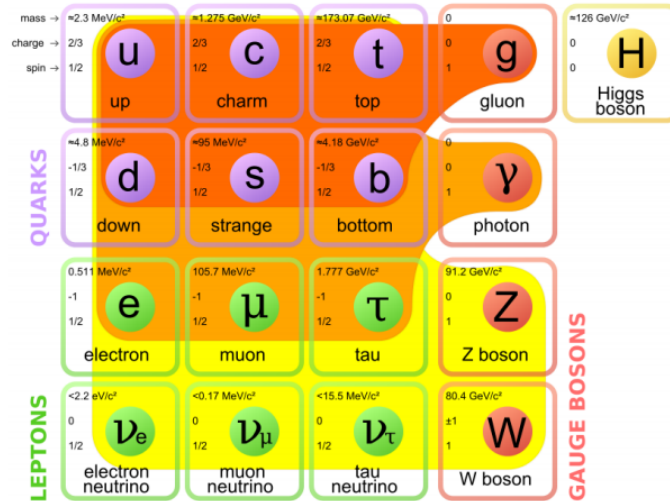


Figure 1: Particle content of the Standard Model of particle physics. The color shades dark orange, orange and yellow indicate which gauge bosons (in red) that couple to which fermions (in purple and green) [8].

2.1.1 Fermions: quarks and leptons

As mentioned above, all matter is made up of spin 1/2 fermions, which are divided into two types: leptons and quarks. The leptons are electrons (e^-), muons (μ^-) and tauons (τ^-), and their respective neutrinos, (ν_e , ν_μ and ν_τ). The leptons come in three generations with two leptons in each generation:

$$\begin{pmatrix} \nu_e \\ e^- \end{pmatrix} \begin{pmatrix} \nu_\mu \\ \mu^- \end{pmatrix} \begin{pmatrix} \nu_\tau \\ \tau^- \end{pmatrix}.$$

The electron, muon and tauon follow a mass hierarchy, where the mass increases with generation. The neutrino masses however, are known to be comparably small ($< eV/c^2$), but non-zero [9].

Quarks are the fundamental objects participating in strong interactions. Until this day, six quark flavors have been discovered and confirmed through high-energy experiments, these are up (u), down (d), charm (c), strange (s), top (t) and bottom (b) (also referred to as beauty). The quarks also organize into three generations as follows:

$$\begin{pmatrix} u \\ d \end{pmatrix} \begin{pmatrix} c \\ s \end{pmatrix} \begin{pmatrix} t \\ b \end{pmatrix}.$$

In contrast to leptons, quarks carry color-charge which gives rise to the strong interaction and confines quarks into bound states, further mentioned in Section 2.1.3. As for the leptons, there is a mass hierarchy between following generations where the up and down generation constitute the lightest quarks and the top and bottom generation contain the heaviest quarks, see Table 1. Due to confinement, quark masses can not be measured directly but are determined indirectly by their effect on the bound state properties. Therefore, dealing with a quark mass one must make reference to the framework that is used to define it [10]. It is common to refer to two different masses of quarks: their "free quark mass", meaning if the quark was actually isolated, and the "constituent quark mass", which refers to the mass it has within the bound state, see Table 1.

Except for neutrinos, all other fermions carry electric charge. Quarks carry fractional electric charge e : all up-like quarks carry $+2/3 e$ and all down-like quarks carry $-1/3e$, where e is the elementary charge ¹. The electron, muon and tauon carry integer electric charge $-1e$.

Table 1: Quark mass table indicating the constituent and free (or bare) masses of the six different types of quarks divided into their three respective generations [10].

Flavor	Constituent mass (GeV)	Free quark mass (GeV)
u	0.336	0.0018-0.0028
d	0.340	0.0043-0.0052
c	1.55	1.30
s	0.486	0.092-0.104
t	177	156-176
b	4.73	4.2-4.7

¹ $e = 1.602 \times 10^{-19} \text{ C}$

In addition to the 12 fermions mentioned, there exist an anti-particle for every fermion. The anti-particles carry the exact same mass as the particle but opposite quantum numbers such as electric charge, lepton numbers and color-charge.

2.1.2 Gauge bosons and the fundamental forces

Fermions do not interact with each other directly, they do so through intermediate agents referred to as gauge bosons, also called force carriers or force mediators. The gauge bosons are listed in the fourth column in Figure 1 and the different shades of orange and yellow indicate which gauge boson that interact with which fermions.

The force carriers of the strong force are gluons (g). Gluons are massless and carry color charge, as do the quarks. Through the combination of the three color charges (and their respective anti-color) there are eight gluons. Gluons only interact with other color-charged particles, hence with quarks or other gluons. This has the implication that particles which do not carry color-charge do not feel the strong interaction. Each color-charge is always conserved in strong interactions and the fundamental theory of the strong interaction is called Quantum Chromodynamics (QCD) which the next section discusses further.

The electromagnetic force is mediated by the photon (γ), and is described by Quantum Electrodynamics (QED) [10]. The photon is massless and only interacts with particles that carry electromagnetic charge, hence with all fermions, except for the charge-neutral neutrinos, and with the charged bosons mentioned further down. The photon itself is electromagnetically charge neutral.

The weak interaction is mediated by three different bosons: the neutral Z^0 and the electromagnetically charged W^\pm bosons. The electroweak bosons are heavy particles with masses $80.1 \text{ GeV}/c^2$ and $91.2 \text{ GeV}/c^2$ for W^\pm and Z^0 respectively. As indicated in Figure 1, the carriers of the electroweak forces interact with all the different fermions. The weak force mediator bosons, together with the photon, comprise the gauge bosons of the unification of the electromagnetic and the weak interactions called the electroweak interactions [10].

2.1.3 Quantum Chromodynamics

Quantum Chromodynamics (QCD) is the theory of the strong force. It is a description of the properties of the color-charged particles, quarks and gluons, and how these interact with each other.

Both quarks and gluons carry the distinct QCD color-charges: *red* (r), *blue* (b) and *green* (g) and their respective anti-colors *anti-red* (\bar{r}), *anti-blue* (\bar{b}) and *anti-green* (\bar{g}). Quarks and anti-quarks carry single color-charges and anti-color-charges respectively, while the gluon carry both color and anti-color. As a result of quarks interacting with and through gluons, color is transferred, but color is always conserved in the interaction [10]. The gluon couples to color-charge, in a similar fashion as a photon couples to electromagnetic charge in QED. However, since the gluons are color-charged, the color of an initial quark state can change due to quark-gluon interaction, a phenomenon that does not occur in

electromagnetic interactions since the photon is charge-neutral.

No isolated colored state has so far been observed, hence no quark or gluon has ever been isolated. This feature of QCD is called *confinement* and means that a quark or gluon can not be taken outside of a confined state. Quarks and gluons are confined within *hadrons*. All hadronic matter are color-neutral states, hence the constituents of the hadrons are combined in such a way that hadrons are colorless. To get a colorless state one either has to combine all possible colors, all possible anti-colors or a color and its anti-color. Which means that the colorless states, hadrons, come in the form of three combined quarks or one quark with an anti-quark. *Baryon* names the state made up of three quarks whereas the state made up of a quark and its anti-quark is a *meson*.

One striking property of QCD is the concept of *asymptotic freedom*, which means that the strong coupling between quarks, α_s , is weakened as the distance between them decreases. At distances of the order of the quark separation within a hadron ($\approx < 1$ fm), quarks appear as free, or *asymptotically free*. Put in another way, the QCD potential between colored states grows with larger quark separation. The QCD potential between two quarks is given by

$$V_{QCD}(r) \approx -c_F \frac{\alpha_s}{r} + kr \quad (1)$$

where c_F is a color factor, α_s is the strong coupling, r the quark separation and k is a spring constant [10]. As seen in Equation 1, at small distances r , V_{QCD} is dominated by the first term, and as the distance r increases the second term dominates and prevents the isolation of color-charged states. The QCD potential confines quarks within hadrons.

Confinement and the asymptotic-freedom-feature of QCD are due to that the force carriers of the strong interaction, the gluons, are themselves color-charged and can *self-interact*. The fact that the gluons can self-interact gives rise to the effect of *anti-screening*. Consider the diagrams in Figure 2. The leftmost diagram shows the effect of screening: a quark emits a virtual gluon which fluctuates into a quark-anti-quark pair before it is absorbed by another quark. The quark pair forming a loop gives rise to a vacuum polarization due to the quark-loop generating a color-field corresponding to the quark color-charges, but with opposite direction to the initial color-field of the initial quark that emitted the gluon. Hence the scattering quarks see less color-charge than if the quark loop would not appear, the color charge is *screened*.

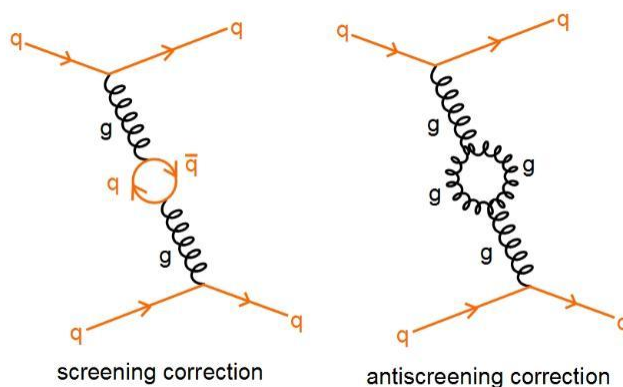


Figure 2: Diagrams illustrating screening and anti-screening effects in QCD [11]

Anti-screening by gluons is the opposite effect of screening, which is shown in the right-most diagram of Figure 2. Here the virtual gluon fluctuates into a gluon pair. Instead of screening, the gluon-gluon pair anti-screens the initial color charge of the scattering quarks through that the color-field generated by the gluon pair runs parallel with the field of the scattered quarks [11]. The effect of the anti-screening, due to the virtual gluons, is that the interaction-strength is enhanced between the two quarks. The effect of gluon anti-screening increases with distance between the scattering quarks, which implies that the strong force strength, α_s , grows with increasing quark-separation.

The concepts of confinement and asymptotic freedom can be exemplified by that the strong coupling constant, α_s , varies with energy scale μ , hence momentum transfer in the interaction process. This is referred to as a *running coupling*. The notion of the coupling constant varying with energy introduces a parameter Λ , which sets the scale at which the coupling becomes large. Considering the QCD scale, $\mu = \Lambda_{QCD} \approx 200$ MeV [7], QCD calculations give the coupling strength as

$$\alpha_s(\mu) = \frac{2\pi}{\beta_0 \ln(\mu/\Lambda_{QCD})},$$

where $\beta_0 = 11 - \frac{2}{3}n_f$ and n_f is the number of quark flavors. Note that $\alpha_s(\mu)$ goes to zero as the momentum scale μ goes to infinity. This behavior of the strong coupling has been verified experimentally in particle physics experiments to very high precisions, as seen in Figure 3.

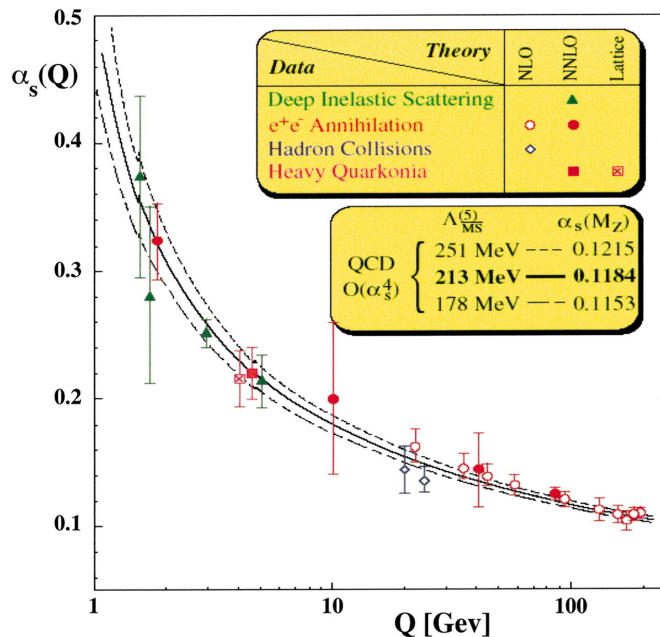


Figure 3: Measurements of the running QCD coupling strength as a function of momentum transfer with experimental data and theoretical predictions indicated [7].

Due to asymptotic freedom, QCD calculations can be performed perturbatively at high energies when the momentum transfer is large [7]. Today, many QCD research results are in the perturbative region where data from high energy physics experiments can be explained by perturbative QCD (pQCD). To further understand QCD better one challenge

of today's high energy physics research is to characterize the behavior of strongly interacting matter at high temperatures and high densities.

Due to quantum fluctuations creating virtual quark-anti-quark pairs, a hadron contains valence quarks, gluons and sea quarks. Collectively, the quarks and gluons are called partons. The quarks which determine the spectroscopic properties and the quantum numbers of a hadron are the valence quarks, also referred to as the constituents of a hadron. However, a hadron can contain any number of additional virtual sea quarks and gluons that do not affect the hadron quantum numbers [10]. The mass of a hadron is not only determined by the valence quarks but also by the virtual sea-quarks and gluons. This is what gives the larger constituent masses as compared to bare quark masses as seen in Table 1.

2.1.4 Strongly interacting matter

At a high enough temperature T and/or high enough baryon chemical potential μ_B , QCD calculations predict a phase transition from hadronic matter to a de-confined strongly interacting state of matter, a state called Quark Gluon Plasma (QGP) [6]. In the QGP the relevant degrees of freedom are partons rather than hadrons. Hence, de-confinement means that the hadrons under the presented conditions turn into a plasma-like state, consisting of asymptotically free quarks and gluons.

For zero baryon chemical potential μ_B , QCD calculations show that the phase transition is a type of cross-over but the critical temperature T_c for the zero baryon chemical potential is not yet known. For μ_B above zero the QCD calculations become more complicated and the phase transition is not yet fully understood. QCD calculations indicate either that the phase transition is still a cross-over or of first order, for non-zero baryon chemical potentials [12]. Today, both the nature of the phase transition and the critical temperature are under investigation. Figure 4 shows a schematic QCD phase diagram for hadronic matter going through a phase transition to a QGP state for high enough temperatures and/or baryon densities.

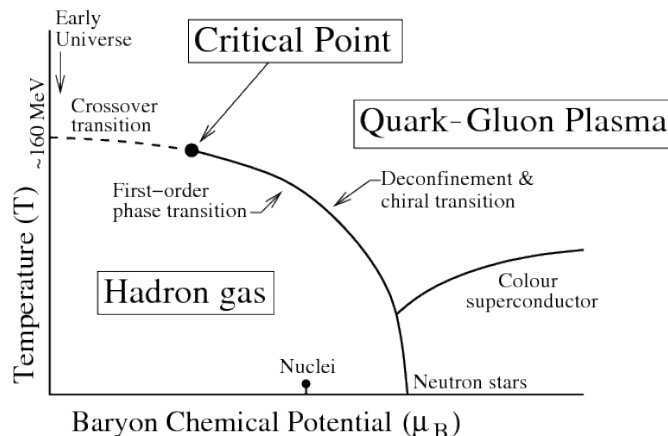


Figure 4: Schematic phase diagram of strongly interacting matter as a function of the temperature T and the Baryon Chemical potential μ_B [13]. The figure indicates where a possible critical point could be in the phase diagram, however it is not yet clear if it exists.

Studies of the strongly interacting QGP is of great interest for the mapping of the QCD phase diagram but also to possibly understand the beginning of our universe. The primordial universe is believed to have spent its first microseconds after the big bang in the state of a QGP at high temperature. As indicated in Figure 4, the early universe went through a transition to hadronization as it expanded and cooled down below the critical temperature T_c . As also indicated in the figure, it is believed that QGP is present today in neutron stars. In the laboratory, high enough energy densities are reached by heavy-ion collisions providing the possibility to study the behavior of the QGP state of matter.

3 Experimental particle physics

The aim of high energy particle collisions is to produce rare, or theoretically predicted, states of matter, for example heavy unstable particles or the QGP state of matter. This is made possible through collisions of elementary particles or nuclei at high energies of the order of 13 TeV. To reach such energy magnitudes particles are accelerated by repeatedly passing varying electric fields in accelerators. There are two types of accelerators available today: linear and circular ones. The more electric fields a particle pass through in the accelerator, the greater energy is available once the collision occurs. Hence, unless a linear collider can be made very long, a circular accelerator enables higher energies at the point of collision, since the particles can pass through the accelerating fields many times by circling around the accelerator. One example of a circular collider is the Large Hadron Collider, further discussed in section 4.

In a circular accelerator the particles are constrained in a circular, or nearly circular, orbit by rows of bending magnets (dipole magnets). Particles traveling on a circular path continuously lose energy in the form of synchrotron radiation. The energy lost, ΔE , by a particle of mass m with an energy E is proportional to the energy E to the power of 4 and to the inverse of the mass m^4 as [14]:

$$\Delta E \propto \frac{E^4}{\rho m^4}$$

where ρ is the curvature radius. As seen in the formula, a smaller mass gives rise to more energy loss due to synchrotron radiation. This motivates the usage of heavier particles, such as protons ($m_p = 938 \text{ MeV}/c^2$), in contrast to using electrons ($m_e = 0.511 \text{ MeV}/c^2$), when the aim is to create large energies at the point of collision.

All hadrons (except for protons) created in high energy particle collisions are unstable particles, meaning that they can and will decay. Preferably a particle decays via the strong interaction, in which the quark number is conserved. If such a decay is not possible, the particle will instead decay electromagnetically or weakly. If possible, a hadron will decay shortly after being created. Hence, the particle is short-lived, as opposed to long-lived or stable. Due to their short lifetimes, short-lived particles, even when created with a velocity close to the speed of light, are able to travel only very short distances, of the order 10^{-15} m (the approximate diameter of a proton) before decaying [14]. The short distance between the interaction point, the *primary vertex*, where the particles are produced and the point where a short-lived particle decays, referred to as the *secondary vertex*, implies that the particle itself cannot be detected, instead one has to study the

decay products of it. To study events in a particle collision and the possible formation of a QGP the distribution of particles formed in the freeze-out phase, as well as particles from the pre-freeze-out phase (such as direct photons), are measured.

3.1 Definitions

Here definitions of variables of high energy physics and specifically heavy-ion physics are introduced. Natural units, $c=1$, are used in the below presented formulas.

3.1.1 Transverse momentum

Momentum is in general divided into two components: p_z , the longitudinal momentum, hence momentum along the beam-line (which defines the z -direction), and transverse momentum, defined as

$$p_T = \sqrt{p_x^2 + p_y^2},$$

where p_x and p_y are the momentum components along the x - and y -direction respectively. The x -direction is perpendicular to the beam-direction and pointing to the accelerator center and the y -direction is perpendicular to the x -direction pointing upward [15]. p_T is Lorentz invariant and is the momentum due to the particle collision, indicating how much the particles are scattered at the collision point. Prior to a collision there is no transverse momentum of the incoming particles and due to momentum conservation, the vector sum of the transverse momentum of particles coming out of the collision should always add up to zero. Characteristically, a hard collision results in high momentum far away from the beam-line direction i.e. a high transverse momentum p_T .

3.1.2 Center-of-mass energy

The collisional center of mass energy is the energy available in a particle collision to create new particles. The center of mass energy is a conserved quantity and can be calculated with the four-momentum vector of a particle: $p^\mu = (E - \mathbf{p})$, where E is the energy and \mathbf{p} the three-momentum of the particle. For two oppositely traveling particles, with equal energy magnitude E , mass m and three-momentum magnitude $|\mathbf{p}|$ the center of mass energy \sqrt{s} is found through:

$$p^\mu p_\mu = (p_1 + p_2)^2 = p_1^2 + p_2^2 + 2p_1 p_2 = (E^2 - |\mathbf{p}|^2) + (E^2 - |\mathbf{p}|^2) + 2(E^2 - |\mathbf{p}|^2) = 4E^2$$

By defining \sqrt{s} as the center of mass energy, this can be expressed as

$$\sqrt{s} \equiv 2E.$$

As seen, for a collision of particles with equal mass, the center of mass energy is twice the energy of the individual beams, as is the case in pp or AA collisions.

3.1.3 Rapidity and Pseudorapidity

At relativistic energies of particles it is useful to define the rapidity y , instead of standard velocity. The rapidity of a particle is defined as

$$y = \frac{1}{2} \ln \left(\frac{E + p_z}{E - p_z} \right)$$

where $E = \sqrt{m^2 + \mathbf{p}^2}$ is the energy of the particle. Rapidity is a dimensionless quantity and a measure of the particle momentum carried in the beamline-direction. In the center-of-mass frame, the region in the proximity of $y = 0$ is called the central rapidity region. Particles in this region are of special interest since they are either new particles resulting from the particle collision or particles already present in the initial beams that have gone through re-scattering processes. Rapidity values $y > 0$ and $y < 0$ indicate if particles move in the forward or backward direction, respectively.

To determine the rapidity both energy and momentum must be measured, which is not always possible. To simplify this, where the mass of the particle is not known, the concept of pseudorapidity η , closely related to rapidity, becomes useful. The pseudorapidity of a particle is defined as

$$\eta = \frac{1}{2} \ln \left(\frac{|\mathbf{p}| + p_z}{|\mathbf{p}| - p_z} \right) = -\ln \left(\tan \frac{\theta}{2} \right)$$

where θ is called the polar angle, the angle the particle trajectory makes with respect to the beam-line direction. Notice that it is enough to measure the polar angle of a particle to calculate the pseudorapidity. For relativistic energies, when the momentum is much larger than the particle mass ($p \gg m$), the rapidity is to a good approximation given by the pseudorapidity.

3.1.4 Impact parameter, centrality and multiplicity

When colliding nuclei, the impact vector is defined as the two-dimensional vector connecting the centers of two particles from different nuclei in the x - y -plane. The length of the vector is called the impact parameter b . A central or peripheral collision corresponds to a very small or large impact parameter, respectively [16]. Multiplicity refers to the number of particles detected in a given collision. Collisions with large multiplicities indicate a large momentum transfer in the collision, while a low multiplicity indicate soft interactions, hence lower momentum transfer between particles.

Characteristically high-multiplicity events are from central collisions and low-multiplicity events are from peripheral collisions. The most interesting QGP-physics is usually found in the most central collisions, with the most participants, highest energies and longest-lived QGP states.

3.1.5 Invariant mass

The invariant mass, or the *rest mass*, of a particle is the mass that remains constant under Lorentz transformations. The invariant mass m_{inv} of a particle can be reconstructed, with

knowledge of the particle's decay products momentum and energy as:

$$m_{inv}^2 = E^2 - \mathbf{p}^2 \quad (2)$$

where E and \mathbf{p} are the total energy and momentum of the decay products respectively. By measurement of the individual energy and momentum of the two daughter particles, 1 and 2, the invariant mass of the mother particle is given by

$$m_{inv}^2 = (E_1 + E_2)^2 - (\mathbf{p}_1 + \mathbf{p}_2)^2 \quad (3)$$

3.2 Heavy-ion collisions

The motivation behind heavy-ion collision experiments is that to a greater degree understand and describe the bulk of particle collisions. As seen above, the strong interaction binds quarks into hadrons and QCD has so far been very successful in describing for example jet production at high transverse momentum [12]. There are however, still unsolved puzzles concerning the strong force theory, such as the understanding of confinement and how masses are generated when quarks are bound together. These types of questions are addressed both where perturbative calculation methods apply and where they do not and together they form the basis of what one aims at to better describe through studies of heavy-ion collisions.

In relativistic heavy-ion collisions the energy per nucleon in the center of mass frame is several thousand times larger than the individual nucleon mass. Particles that interact with particles of another nucleus in a collision are referred to as *participants* whereas particles that do not are called *spectators*, see Figure 5.

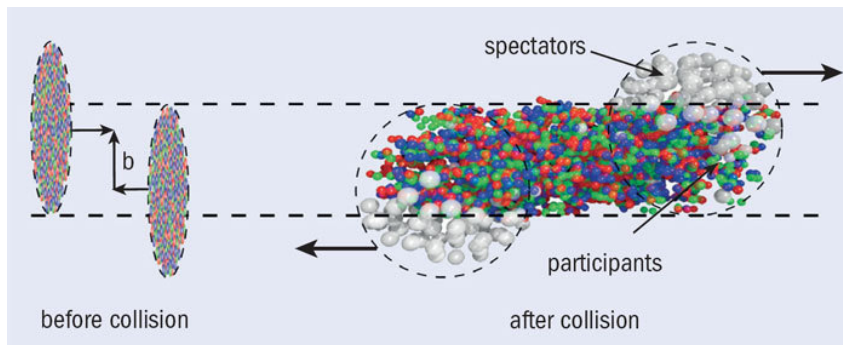


Figure 5: Simplified picture of before and after, in a heavy-ion collision. In the figure the impact parameter b , the spectators and the participants are indicated. [17]

Participants in an AA collisions produce color-charged partons that develop into color-strings which fragment into detectable hadrons. The number of particles created in such a collision is to a good approximation proportional to the number of participants, N_{part} [12]. However, a participant can collide with several nucleons of the other nucleus. The number of nucleon-nucleon (NN) collisions is referred to as the number of binary collisions N_{bin} .

The dominant process in high-energy heavy-ion collisions is inelastic scattering between the participants. As nuclei are accelerated to relativistic speeds they are Lorentz contracted before the collision. At the time of collision, hard and soft interactions occur

between the participants. The hard collisions happen when partons interact with large momentum transfer. The collisions result in high p_T quarks and heavy quarks. Soft collisions are interactions between color-fields with smaller momentum transfer, forming a collective partonic medium in which the strong force is dominant, resulting in the creation of quarks, anti-quarks and gluon pairs. The partonic medium is extremely dense and hot and has been found to have liquid-like properties such that it expands in space when undergoing the phase transition to a QGP. As the QGP expands in space it cools down and finally reaches the freeze-out phase in which quarks and gluons are forming hadrons [18]. The QGP is a regime without confinement and with quarks at their bare masses and the creation of such a state in the laboratory provides a way of studying QCD. Results from heavy-ion collision experiments have been able to pin down properties assigned to the QGP, such as collective particle motion and enhancement of strange particle production [12].

3.2.1 A de-confined state of matter

Heavy nuclei collisions give rise to high enough energy densities to create a fireball in which the QGP forms and the goal of heavy-ion collision research is to experimentally investigate the hot and dense QCD phase in the laboratory. The fireball is hot and dense enough for the quarks and gluons in it to equilibrate in less than 1 fm/c [12]. Great pressure gradients then put the system in a hydrodynamical phase which expands, cools down and finally reaches a hadronization phase. As the system gets cold enough the hadrons go through a freeze-out phase and eventually, much later, reach the detectors. The QGP is expected to have a very short lifetime, of the order of a few fm/c, and a 5 to 10 fm extension in space [18], which implies great challenges for studies of the QGP through detection of particles with detectors at distances of the order of 10^{-2} to 1 m away from the collision point.

In the QGP phase of matter the degrees of freedom of the partons in the QGP are higher than if the partons would be bound and confined within hadrons. Above the critical temperature T_c the quark-anti-quark pair creation is enhanced and the constituents of a pair are due to the pressure in the fireball separated from each other and the partons will act as if they did not belong to a specific hadron. Therefore the QGP state of matter is described as a phase of *deconfined* but strongly interacting matter [12]. Within the QGP, color-charge is screened by color-charged loops of quarks, similar to the loops in Figure 2, and quarks and gluons will not be able to form hadrons. The QGP is expected to manifest itself through different signatures such as suppression of highly energetic partons, collective parton motion, enhancement of strange particle production and various probes of de-confinement.

One distinguishes between modifications in the form of initial state effects and final state effects, where initial state effects are due to the fact that nuclei are large and complex states as compared to nucleons. Hence initial state effects take into account that parton distributions in nuclei are different from the distributions in nucleons. Final state effects refer to effects due to the formation of a QGP.

3.2.2 QGP signals

Hard scattering processes depend on the number of binary collisions (N_{bin}) collisions and since there are more nucleons participating in an AA collisions, more hard-scattering processes are expected to occur in AA-collisions as compared to pp collisions. In pp collisions, there are two participants and one binary collision, whereas in AA-collisions the number of collisions scale with the number of nucleons in each nucleus, hence a greater number of binary collisions. An AA-collision can be seen as a superposition of NN collisions, and the differential particle yield of an AA collision is given by

$$dN_{AA}/dp_T = N_{bin} \cdot N_{pp}/dp_T,$$

where dN_{pp}/dp_T denotes the invariant particle yield in pp collisions. The fraction of dN_{AA}/dp_T and $N_{bin} \cdot dN_{pp}/dp_T$ is an observable called the nuclear modification factor:

$$R_{AA} = \frac{dN_{AA}/dp_T}{N_{bin} \cdot dN_{pp}/dp_T}. \quad (4)$$

R_{AA} is a measure of medium induced modifications and R_{AA} is consistent with unity, when no modification appears, i.e. if no initial or final-state effects are present and the approximation that the AA collision is a superposition of NN collisions holds. A value of R_{AA} deviating from one, indicates a modification of the particle production and hence that the AA collision production does not scale with NN collision yields. Measurements of R_{AA} enables deduction of properties of the medium created in AA collisions where pp collisions are used as a reference [12].

For collisions with non-zero impact parameter the geometry of the fireball created in the collision is asymmetric and takes on an ellipsoid-shape. This creates asymmetric pressure gradients within the fireball and the spatial anisotropy translates into azimuthal anisotropy in momentum space of the final state. In momentum space, the anisotropy can be quantified by a Fourier expansion of the momentum distribution of the state generating harmonic coefficients, also referred to as flow-coefficients, recognized as being sensitive to the initial state of the created fireball. By qualitative study of the flow coefficients it has been found that the equation of state of the initial QGP expands collectively like a perfect fluid, with small shear viscosity to density ratio [12].

Another signature of the QGP state of matter is that quarks and gluons created in early partonic hard scattering processes, i.e. jets, suffer great energy loss as they pass through the QGP, a process called *jet quenching*. Jet quenching results in the suppression of hadrons from jet fragmentation as compared to that of a superposition of independent NN collisions. The suppression is quantified by the nuclear modification factor, as given in Equation 4, being lower than unity [12].

Charm and bottom quarks, collectively referred to as heavy-flavor, have bare quark masses $m_c = 1.29$ GeV and $m_b = 4.19$ GeV (which makes them the heaviest fundamental fermions, except for the top quark, see Table 1), that significantly exceeds the QCD scale parameter $\Lambda_{QCD} \approx 200$ MeV [12]. Due to their large masses, c and b are exclusively produced in hard parton-parton scattering which occurs in the initial phase of the collision. As the heavy-flavor quarks move in the QGP medium, they carry information about the medium and measurements of these states are used to characterize the QGP.

Measurements of heavy-flavor production in pp collisions provide tests of perturbative QCD calculations and serve as a benchmark for measurements in heavy-ion collisions, the denominator in Equation 4. In the project here presented the goal has been to study the production of heavy-flavor quarks in pp collisions, measured at the LHC with the ALICE detector.

3.2.3 Heavy-flavor as a signal of QGP

Without nuclear effects present in AA collisions, heavy-flavor production is expected to scale with the number of binary collisions N_{bin} . Previous measurements [12] have shown that there are deviations from such scaling so that heavy-flavors are used to quantify nuclear modifications. Final state effects are expected to be highly dependent of the energy density of the QGP medium, which is supposed to manifest itself through that high p_T distributions of heavy-flavor hadrons and their decay products are softened in AA collision as compared to pp collisions. Hence, final state effects are expected to change the heavy-flavor and heavy-flavor-decay product distributions [12].

Meson states of c and anti- c or b and anti- b quarks are referred to as quarkonia, or hidden heavy-flavor states, since these states are flavorless as the quark and anti-quark flavor quantum numbers cancel out. As opposed to hidden-heavy-flavor, open heavy-flavor states refer to hadrons with heavy-flavor quantum numbers. The quarkonium production in heavy-ion collisions is sensitive to the QGP medium temperature and the de-confinement within the medium, due to quarkonium different binding energies [19]. Quarkonia state production are expected to be suppressed due to QGP de-confinement but the production is also supposed to be sensitive to re-generation processes due to the many heavy-flavor states produced in heavy-ion collisions [12].

Yield suppression of quarkonia, meson states of c - and b -quarks, was for a long time proposed as an observable of de-confinement in the QGP [19]. Color charge screening in the de-confined medium was suggested to prohibit c and anti- c to form the bound state named a J/Ψ particle. The expected suppression of J/Ψ yield was observed in central lead-lead (PbPb) collisions at CERN SPS [20]. On the other hand, the suppression could also be described by absorption of quarkonia states due to cold nuclear matter effects or by the bound states having been broken by scattering with hadrons produced in the collisions, which does not require de-confinement. Hence the observed suppression lead to ambiguous interpretations. Also, the realization of de-confinement effects possibly leading to enhanced quarkonium production, or re-generation, at high enough heavy-flavor particle production, again lead to ambiguous interpretations of data observed at first at SPS [12].

In collider experiments, such as PbPb collisions at LHC, with greater energy, more than 100 (so far) pairs of c and anti- c quarks can be produced in initial collisions where the number of present heavy-flavor particles are enough to turn a J/Ψ suppression into enhancement through re-generation processes [12] [21]. Indeed the proposed re-generation of quarkonium states have so far been observed, where the nuclear modification factor of J/Ψ at forward rapidity is larger in central AA collisions at a higher collision energy as compared to those of a lower collisions energy, which suggest a re-generation of quarkonia in the de-confined QGP environment [12].

Figure 6 shows an example of J/Ψ suppression by the nuclear modification factor for J/Ψ production as a function of centrality. The R_{AA} dependency on centrality shows an increasing suppression with centrality up to $N_{part} \approx 100$, and at higher centrality an almost constant R_{AA} distribution.

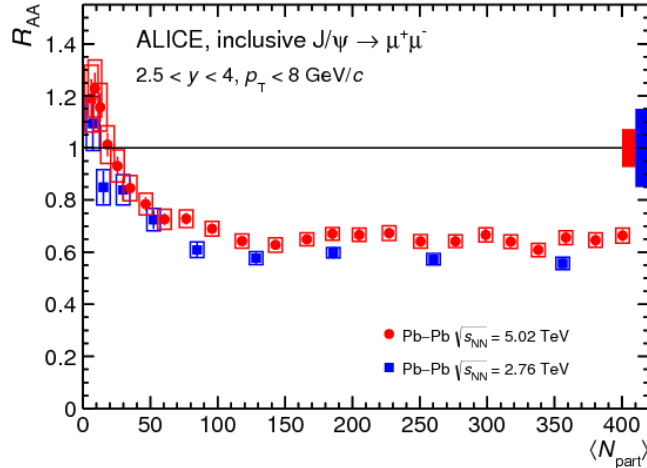


Figure 6: Nuclear modification factor for J/Ψ yield as a function of centrality, in PbPb collisions at $\sqrt{s} = 5.02$ and $\sqrt{s} = 2.76$ TeV, measured with the ALICE detector [22]

Heavy-flavor production is studied through measurements of hadrons carrying c - or b -quarks or by measurements of their daughter particles. Open heavy-flavor production rates provide a reference to quarkonia states but also measurements of the energy density of the QGP medium, since the open heavy-flavor yield is sensitive to the presence of the QGP [12].

The interaction of partons with the QGP is suggested to be sensitive to the QGP medium energy density through the process of parton energy loss. Since the QGP medium has a high density of color sources, quarks and gluons, the quarks and gluons that traverse the QGP will feel the color-charge fields. Energy of the traversing particles is lost dominantly in two different ways. Firstly, collisional energy loss, hence elastic scatterings, which dominate at low momentum. Secondly, radiative energy loss from inelastic scatterings, which dominates at high momentum and through gluon bremsstrahlung, which happens when a gluon is radiated out and changes the momentum of the initial parton [12].

Because gluons have a larger color-coupling than quarks, gluons are expected to lose more energy than quarks [12]. This suggests a mass hierarchy in the radiative energy loss. At transverse momentum up to the order of heavy-quark masses being comparable to their momenta, energy loss is expected to decrease in the order from lighter flavor hadrons, dominantly from gluon or light-quark jets, to hadrons containing c and b quarks. The energy mass hierarchy suppression is described by the nuclear modification factors, as given by Equation 4 and gives the following hierarchy of suppression:

$$R_{AA}^{\pi} \ll R_{AA}^c \ll R_{AA}^b$$

where R_{AA}^{π} is an example of the nuclear modification of a light-quark hadron, a pion π . In terms of energy loss (ΔE) the following hierarchy holds:

$$\Delta E_{\pi} \gg \Delta E_c \gg \Delta E_b \quad (5)$$

where again, a pion exemplifies the fact that a lighter quark loses more energy as compared to heavy-flavor quarks, when propagating through the QGP.

Additionally, Cold Nuclear Matter effects (CNM) can lead to enhancement or suppression of heavy-flavor yields in heavy-ion collisions. In order to disentangle all the different types of effects, there is a need to study a wide variety of heavy-flavor species and probes in wide p_T ranges in both, pp, pA and AA collisions.

In summary, the contributing effects to the yield of heavy-flavor in hadronic collisions is not easily disentangled. pp collisions provide a unique way of testing QCD and forms an experimental reference to the same yields found in heavy-ion collisions. As seen, in heavy-ion collisions the interaction of heavy c- and b-quarks is expected to quantitatively and qualitatively be different from the interaction of light quarks and gluon jets in the QGP environment. Hence, heavy-flavor production measurements provide a complementary characterization of the parton-medium interactions within QGP and of the properties of strongly interacting matter. These measurements are an important part of the future program for ALICE (A Large Ion Collider Experiment) at CERN, in particular motivating the 2019-2020 ALICE upgrades.

4 The ALICE experiment at the LHC

The Large Hadron Collider (LHC) is the world's largest circular particle accelerator, providing the highest energy today in particle collisions [23]. The LHC was proposed and constructed by the European Organization for Nuclear Research (CERN) and is designed to collide protons and lead ions to address fundamental questions in physics research. At the LHC there are four different interaction points for experiments: ALICE [1], ATLAS [24], CMS [25] and LHCb [26]. ALICE, an acronym for A Large Ion Collider Experiment, is the detector optimized for measurements of lead-lead (PbPb) collisions and in particular for the study of QCD matter under extreme conditions.

The LHC is situated in a 26.7 km long tunnel approximately 100 m below ground, across the border between Switzerland and France. Particle collisions occur between particles of the same charge in two parallel beam pipes where proton or ion beams travel in opposite directions and intersect at the four interaction points.

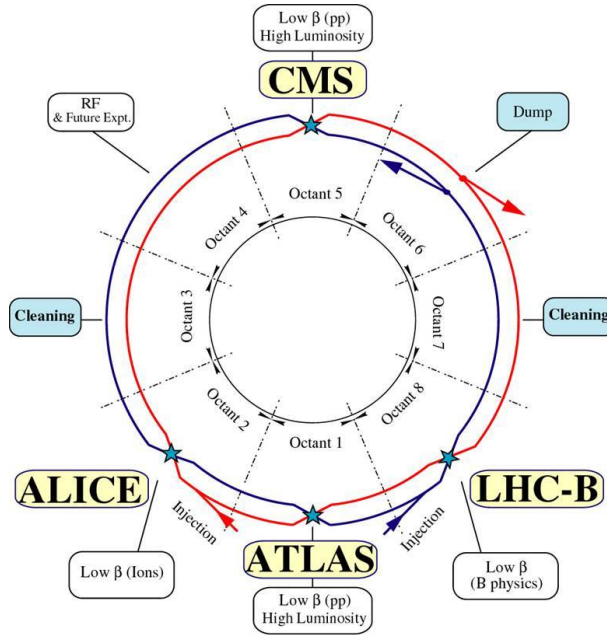


Figure 7: A schematic picture of the LHC layout indicating the four interaction points: ALICE, ATLAS, CMS and LHCb [27]

More than a thousand dipole magnets are used to keep the particle beams on their circular path and more than three hundred quadrupole magnets are used to focus the particle beams, maximizing the probability of collision at the intersection points where the particle beams cross each other [23]. Before entering the LHC the protons and nuclei are pre-accelerated using linear accelerators and then fed to the Proton Synchrotron (PS) and the Super Proton Synchrotron (SPS). From the PS and the SPS the particle beams are transferred to the LHC-rings where they are accelerated up to their collision energies and stored for several hours.

LHC operations are divided into periods of data taking which are followed by shutdowns, during which upgrades and maintenance are performed both to the LHC ring and the detectors. Run 1 refers to the first period of data taking which took place between the years 2009 and 2013. Data sets with detailed heavy-flavor production with pp collisions at $\sqrt{s} = 7$ TeV were for the first time recorded by all experiments at the LHC in 2010 and 2011. By scaling of the $\sqrt{s} = 7$ TeV pp data to the first PbPb data recorded at $\sqrt{s} = 2.76$ TeV, pp data have been used as a reference for the PbPb-data. In 2012 the nominal center of mass collision energy reached $\sqrt{s} = 8$ TeV for pp collisions. During the shutdown between the years 2013 and 2015, maintenance was performed for the LHC to enable pp collisions at 14 TeV. Run 2 started in 2015 and will end in 2018, for upgrades of the experiments during 2019-2020. The nominal center of mass energy so far reached in 2016 was $\sqrt{s} = 13$ TeV and so far all pp-data measurements of heavy-flavor at the LHC are in agreement with QCD predictions [12].

4.1 The ALICE experiment

ALICE is the detector dedicated to research on heavy-ion collisions at CERN and more specifically to study the QGP state of matter. The ALICE detector is optimized for high

charged-particle multiplicities and particle identification over a broad range of momentum, which arise in heavy-ion collisions. Following, the QGP freeze-out the particles and decay products resulting from the collisions are reconstructed and detected using different sub-detectors of the ALICE detector. Complementary to measurements of PbPb collisions, ALICE also measures pp and pPb collisions for reference measurements in order to distinguish effects due to QGP from other sources.

Figure 8 shows a schematic layout of the ALICE detector, which is 26 m long, 16 m high, 16 m wide and situated 56 m below ground. The central barrel is made up of several sub-detectors. Closest to the beam line, the trackers constituting the Inner Tracking System (ITS) and the Time Projection Chamber (TPC) are placed. ITS is placed closest to the interaction point and is designed for high precision determination of collisional and decay vertices and particle tracking. In the ITS, primary vertices are reconstructed by the Silicon Pixel Detector (SPD). Additionally, track measurements in the ITS are used to improve momentum resolutions obtained in the TPC. The TPC is the main tracking element and is built to reconstruct three-dimensional trajectories of charged particles, providing particle identification (PID) through specific energy loss (dE/dx) measurements. The Transition Radiation Detector (TRD) is used for tracking and identification of charged particles by transition radiation and specific energy loss. With the Time of Flight (TOF) detector particle velocities at intermediate momenta are measured, which provide PID. The Electromagnetic Calorimeter (EMCal) is used for detection of photons and electrons to determine the energy of outgoing charged particles. The Photon Calorimeter (PHOS) and the High Momentum Particle Identification Detector (HMPID) are also situated together with EMCal as the outermost layer of the central barrel. The ITS, the TPC and the TOF all cover the entire azimuthal angle and a pseudorapidity range of approximately $-0.9 < \eta < 0.9$. The central barrel detectors are enclosed within a solenoidal magnet with a 0.5 T magnetic field.

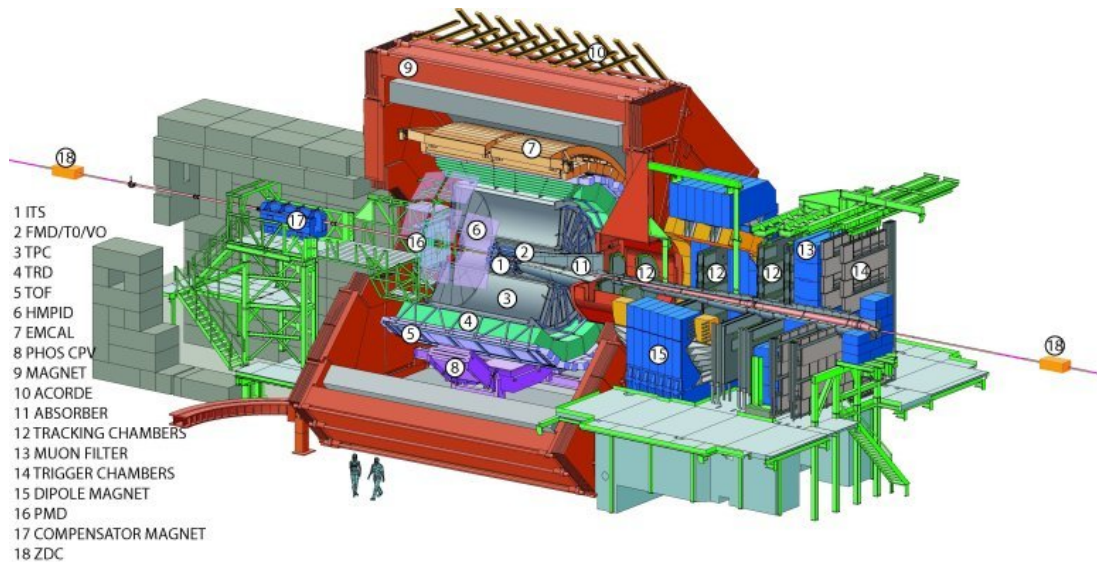


Figure 8: Schematic layout of the ALICE detector [28]

The Photon Multiplicity Detector (PMD) and the Forward Multiplicity Detector (FMD) are situated in the forward rapidity region. The T0 detector is designed to measure the

longitudinal position and time of interactions and the V0 detector is designed for triggering on events and providing event centrality together with forward calorimeters (ZEM and ZDC). The electromagnetic calorimeter (ZEM), also placed in the forward rapidity region, is designed to distinguish between most central and most peripheral events and for further measurements of event centrality the Zero Degree Calorimeter (ZDC) is used. High p_T muons are detected with the forward muon spectrometer also situated in the forward rapidity region.

4.1.1 The Time Projection Chamber (TPC)

The main tracking detector at the central rapidity of the ALICE detector is the Time Projection Chamber (TPC) used for tracking and identifying charged particles. The device surrounds the beam pipe and consists of a cylindrical chamber with a volume of 90 m^3 . The axis of the chamber is aligned with the LHC beam-line and is parallel to the magnetic field. Figure 9 shows a schematic picture of the TPC design where the active volume of the chamber is filled with a gas mixture of Ne, CO_2 and N_2 and within it an axial electric field is present.

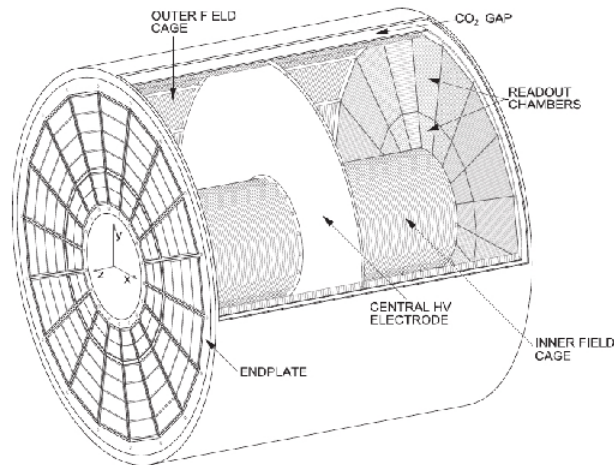


Figure 9: Schematic layout of the Time Projection Chamber [28]

As charged particles pass through the chamber, the gas atoms are ionized and the liberated electrons drift in the electric field. By detecting the electrons with Multi-Wire Proportional Chambers (MWPCs) at each end of the TPC, and by measurement of the particle drift time, a three-dimensional track image of the ionizing particle is reconstructed. The x - y - component is obtained from MWPC data, while the z -component is reconstructed using the drift time and the known drift velocity.

The charged particles drift towards the MWPC anodes where they are accelerated to higher speeds. The acceleration causes an electron to create an avalanche of ionized particles and electrons as they ionize the gas further. An electron reaching the anode induces a signal in one or more pads which is registered by the MWPC. As several pads of a single row register the particle, a cluster is created. Due to the limited number of pad rows, a maximum of 159 clusters can be created for each particle. Small dead parts exist between

the sectors of anodes where no ionization can be detected [28].

The average specific ionization energy loss per unit path length of a particle, dE/dx , is also measured in the TPC. The specific energy loss is a measurement of how much energy the detected particle loses over a distance dx due to Coulomb interactions with the atoms in the gas and is a statistical process theoretically described by the Bethe-Bloch function:

$$\frac{dE}{dx}(\beta\gamma) = \frac{4\pi N e^4}{m c^4} \frac{1}{\beta^2} z^2 \left(\ln \left(\frac{2 m c^2}{I} \right) \beta^2 \gamma^2 - \beta^2 - \frac{\partial(\beta)}{2} \right) \quad (6)$$

where $\beta\gamma = p/m$, i.e. γ is the Lorentz factor, $\partial(\beta)$ is a density effect correction term, I the mean excitation potential of the material that the particle traverses, $m c^2$ the rest energy of the particle, z the particle charge and N the electron number density of the material. The magnetic field present within the TPC causes charged particles to travel in curved trajectories in the x - y -plane, also referred to as the azimuthal plane, which is used to determine the momentum of the reconstructed tracks.

Figure 10 shows the ionization energy loss dE/dx as a function of p for pp collisions at $\sqrt{s} = 7$ TeV measured with the TPC in the ALICE detector. In the figure, TPC tracks consistent with pions, kaons, protons, deuterons and electrons are visible.

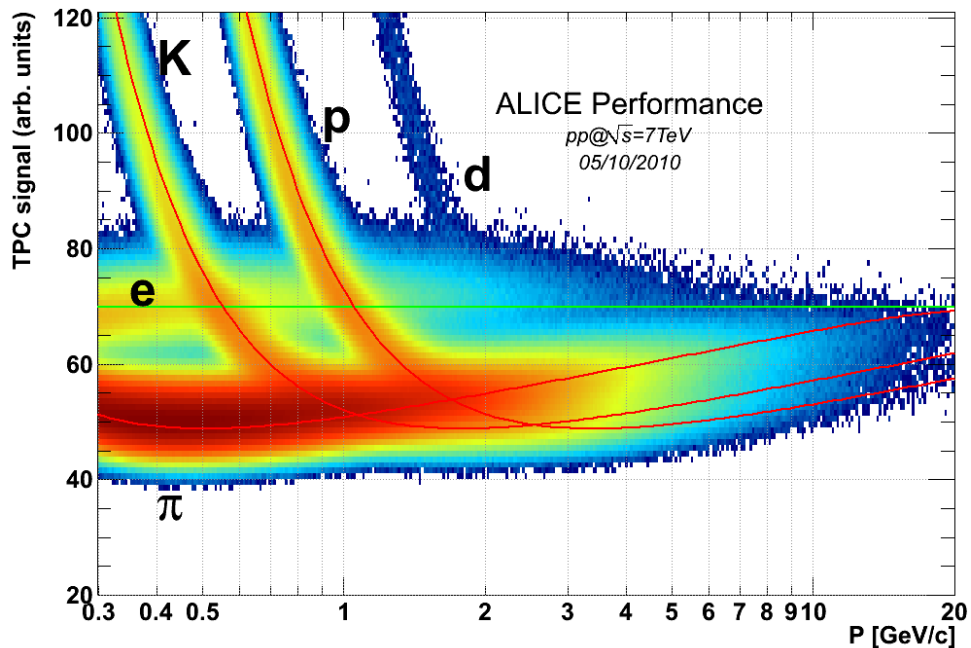


Figure 10: The ionization energy loss (dE/dx) as a function of p as measured with the TPC in ALICE used for PID. TPC tracks consistent with pions, kaons, protons, deuterons and electrons are displayed [29].

4.1.2 The Electromagnetic Calorimeter (EMCal)

Outside of the TPC and the TRD the Electromagnetic Calorimeter (EMCal) is situated, which is designed to measure the particle energy deposited in it. The EMCal's prominent features are that it enables discrimination of electrons from hadrons and enables measurements of the energy of neutral particles, which in turn enables jet reconstruction.

Additionally, EMCal is used for measurements of photons which are used for the reconstruction of neutral hadrons.

As a particle hits the EMCal an electromagnetic shower is initiated, emitting electron and positron pairs and photons. The electromagnetic shower propagates through the calorimeter and deposits its energy throughout the detector until it eventually stops or reaches the boarder of it. EMCal is a lead scintillator calorimeter, designed to dominantly measure electron and photons coming out of the particle collision. However charged hadrons can also interact with it. This mainly occurs in the form of interaction with atoms of the detector, due to strong interactions. Most likely though, hadrons will traverse the EMCal and not be detected in this part of the detector. In contrast to hadrons a shower from an electron is fully contained and measured by the EMCal.

The EMCal is a sampling calorimeter, and is made up of 77 layers of alternating lead and scintillators. The detector spans $\eta = -0.7$ to $\eta = 0.7$, has an azimuthal acceptance of about 107° and is segmented into 12672 towers [3]. A particle passing through the EMCal produces an electromagnetic shower of photons in the lead which is measured by the scintillators. The photonic signal produced in the scintillators is collected by fiber optics and converted into an electric signal, via Avalanche Photodiodes (APDs). Figure 11 shows a schematic picture of the layout of the EMCal where the tower segments are shown in green.

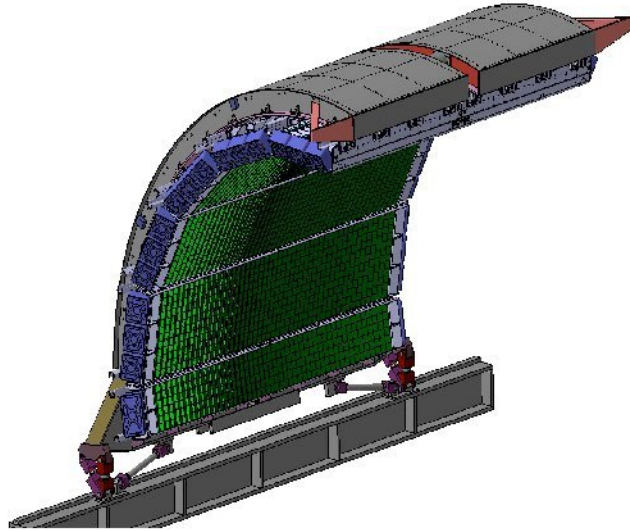


Figure 11: Schematic layout of the EMCal detector [30].

5 Method of Analysis

The analysis outlined here has been constructed in two independent parts: one spectra analysis and one DCA (distance of closest approach) distribution analysis. In the spectra analysis, electron candidates are selected based on electron identification. Subsequently, non electron background and electrons from photon conversions have been identified and subtracted. The final sample gives the yield of electrons from heavy-flavor decays. The analysis has been complemented by an efficiency estimation where reconstructed MC data electron candidates were compared to True MC identified electrons and reconstructed MC has been compared to real data electron yields as a function of p_T .

To study the expected fraction of heavy-flavor semi-leptonic decay electrons the DCA_{xy} distributions were studied. The analysis makes use of reconstructed MC simulations where track particle type and mother particle types are known. By use of true electrons identified in simulated MC the fractions of electrons from charm- and bottom-hadrons as compared to the total number of produced true electrons have been identified. Further the same known particle type DCA_{xy} distributions have been used to try to fit the heavy-flavor hadron decay electrons to electrons identified in data.

5.1 Data, software used and event selection

The analysis presented here has been constructed in C++ and carried out in the AliROOT data analysis framework, which is a custom environment of ROOT [31], specifically designed for ALICE. The analysis is performed using real data, reconstructed MC simulations and generated MC simulations. The real data are extracted from year 2016 Run 2 pp collisions at LHC, at a center of mass energy $\sqrt{s}= 13$ TeV, for all impact parameters, recorded by the ALICE detector. The data consists of 44 million events that contain tracks, where each and every track corresponds to one detected particle as reconstructed by the detector.

In the same fashion as for data, MC events also contain tracks which corresponds to particles, but where the particles and their interactions have been simulated with Pythia [32]. Subsequently, reconstruction of MC events has been done with Geant3 [33], for transport of the generated particles and simulation of detector-like conditions and triggers, imitating those of the ALICE detector. The MC simulations used here contain 42 millions events of simulated pp collisions at $\sqrt{s}= 13$ TeV. In the following, MC Rec refers to the reconstructed MC events which have gone through the same event and track selection as the real data. All *true* particles, such as true electrons, are tracks of the MC Rec identified using PDG markers [34]. For the efficiency corrections the generated MC, in the following referred to as MC Gen, has been used.

All events selected for analysis are required to have at least one hit in the SPD of the ITS. The number of pile-up events, events with multiple pp collisions, are minimized by requiring that the primary vertex as reconstructed in the SPD to be within 0.5 cm of the primary vertex along the beam-axis. Further, all events are required to have a primary vertex no further than 10 cm away from the primary vertex, along the beam-axis and no further than 0.3 cm away in the transverse direction.

5.2 Electron mother-particle analysis

As a representation of the expected p_T distributions of electrons from leptonic decays of heavy-flavor, reconstructed MC data with available particle identification and mother-particle identification were studied. Electrons were identified using Particle Data Group (PDG) markers followed by usage of the mother PDG markers for the identified electrons. The identified heavy-flavor mother particles are listed in Table 2.

Figure 12 shows the p_T distributions of the identified electrons with indicated mother particles where (a) the mother particles of the identified electrons are divided into five different groups and (b) where the mother particles of the electrons are divided into three different groups. The "other hadron" group of Figure 12 (b) is dominated by mother particles of the types π -mesons, Kaons, η mesons, ρ -mesons, ω -mesons, ϕ -mesons and Σ -baryons. The lepton group includes electrons, muons and tauons, and the heavy-flavor hadrons contributing to the electron production are listed in Table 2.

Table 2: Heavy-flavor hadrons used for MC identification

Particle	Quark content	Mass (GeV/ c^2)	$c\tau$ (μm)	pdg code
J/Ψ	$c\bar{c}$	3.096916 ± 0.000011	≈ 0	443
D^+	$c\bar{d}$	1.86961 ± 0.00009	311.8	411
D^0	$c\bar{u}$	1.86484 ± 0.00005	122.9	421
D_s^+	$c\bar{s}$	1.96847 ± 0.00033	150.2	431
Λ_c^+	udc	2.28646 ± 0.00014	59.9	4122
Ξ_c^+	usc	$2.4678^{+0.0004}_{-0.0006}$	132	4232
Ξ_c^0	dsc	$2.47088^{+0.00034}_{-0.0008}$	33.6	4132
Ω_c^0	ssc	2.6952 ± 0.0017	21	4332
$\Upsilon(1S)$	$b\bar{b}$	9.4603 ± 0.00026	≈ 0	553
B^+	$u\bar{b}$	5.27929 ± 0.00015	491.1	521
B^0	$d\bar{b}$	5.27961 ± 0.00016	455.7	511
B_s^0	$s\bar{b}$	5.36679 ± 0.00023	453.3	531
Λ_b^0	udb	5.6202 ± 0.00016	422.7	5122
Ξ_b^0	usb	5.7919 ± 0.00005	426	5232
Ξ_b^-	dsb	5.7945 ± 0.00014	426	5132

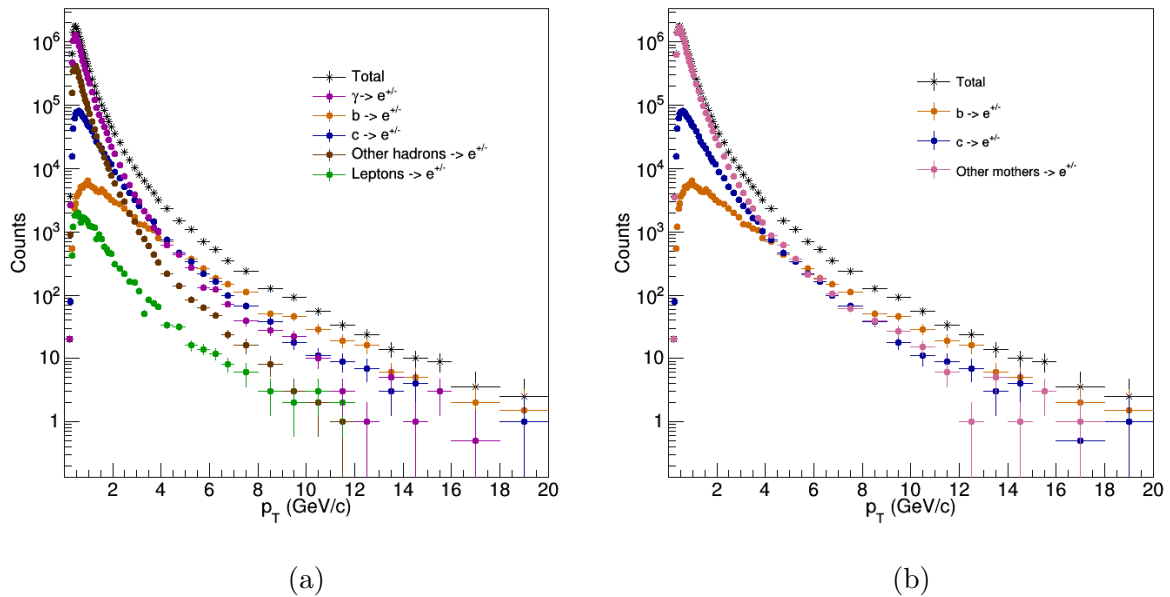


Figure 12: (a) p_T distributions of electrons from b- and c- weak hadron decays, as well as from decays of lighter hadrons, photons and leptons obtained with reconstructed MC simulations in the p_T range $0 < p_T < 20$ GeV/c. (b) shows the same b- and c- hadron distributions as in (a) but with all other mother particles bunched together as "other mothers". The distributions are normalized to the bin width.

Figure 12 (a) shows that for low p_T ($p_T < 4$ GeV/c) the dominant production of electrons are due to other sources, such as photon conversions as well as the decay of lighter hadrons. Hereafter comes the c-hadron decays contribution to the low p_T electrons, followed by b-hadron decays and last the leptonic decay contribution, which is low for the full p_T range studied. For higher p_T values ($p_T > 4$ GeV/c) the total production of electrons is to a greater degree dominated by charm and bottom decays. This is also visible in Figure 12 (b), where the mother particles of the electrons are divided into three groups, b, c hadrons and *other mothers*, where the last group includes all other mother particles except for the charm and bottom hadrons. It should be noted that for higher p_T values the production of electrons goes down rapidly, which indicates lower statistics available for such p_T ranges.

Following the division of mother particles as indicated in 12 (b), the ratio of tracks identified as electrons within each group and total electron production has been studied as a function of p_T . Figure 13 shows the fractional yield of b, c and other mother electrons.

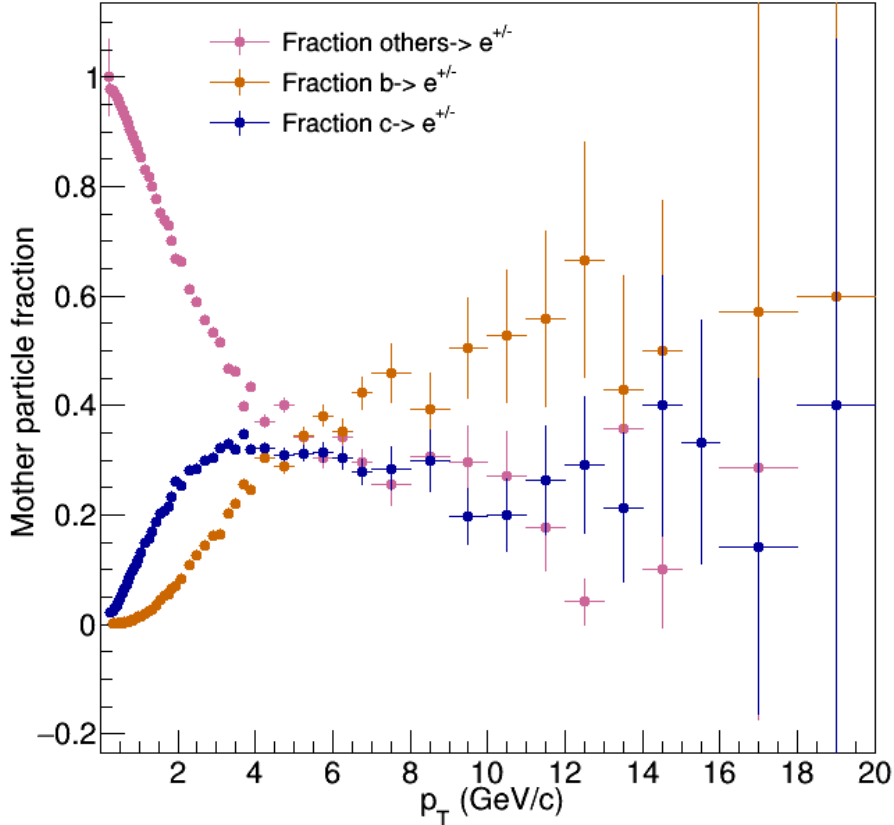


Figure 13: MC electron mother particle fractions with b, c and other mother particle fractions divided by total number of electron yields, as a function of p_T .

Again, it can be seen in Figure 13 that with an increasing transverse momentum p_T , above $p_T \approx 4$ GeV/c, the dominant number of hadrons come from heavy-flavor hadron decays. This implies that a further analysis of the heavy-flavor hadron production by the use of electron tracks should be made for these higher p_T ranges, in order to eliminate dominant contributions from other particle decays to electrons.

5.3 Track selection

Initial track selection was made by cuts on tracks of events that made it through the event selection. All tracks were required to be within $|DCA_{xy}| < 2.4$ cm, in the plane transverse to the beam direction, and $|DCA_z| < 3.2$ cm along the beam direction. All electron tracks were required to be within a pseudorapidity acceptance of $|\eta| < 0.6$.

5.4 Electron identification

For identification of electrons from heavy-flavor, the specific ionization energy loss (dE/dx), measured in the TPC, momentum p , measured in the tracking system, and the energy E , deposited in EMCal, of each track was used.

Figure 14 shows the distribution of dE/dx as a function of p_T for pp collisions at $\sqrt{13}$ TeV, which was used for this analysis, as measured in the TPC, for all tracks passing

initial track selection. All electron candidate tracks were selected by an applied cut on the specific ionization energy loss dE/dx in the TPC. The electrons are visible as a band of tracks with transverse momentum close to a constant $dE/dx \approx 80$. However, as seen in the figure, other particles contribute to this part of the spectrum, especially for low p_T values ($p_T < 1 \text{ GeV}/c$), where also most of the electron tracks appear. For this purpose, to get a clean sample of electrons, only a small part of the dE/dx distribution was used to identify the mean and the spread of dE/dx for electrons.

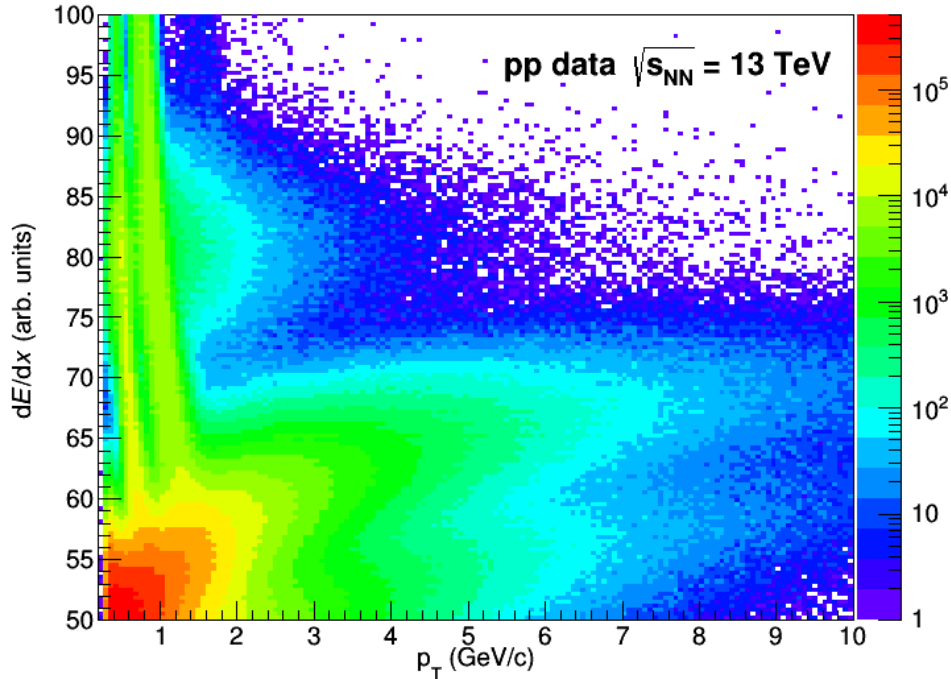


Figure 14: dE/dx as a function of p_T measured with the TPC.

The electron dE/dx mean, along with the standard deviation σ , was found through a gaussian fit between $dE/dx = 71$ and $dE/dx = 91$ of the dE/dx distribution. The fit was applied on the dE/dx distribution in Figure 14, in a p_T range where the sample is for the most part clean from other particles (in $1.5 < p_T < 2.6 \text{ GeV}/c$). The gaussian fit was applied to the dE/dx distribution for each p_T bin in the designated range, which added up to a total of 17 p_T bins. The dE/dx mean for the electrons, $\mu_{electron}$, was calculated as the average of the means found for each p_T bin studied. The mean dE/dx for electrons was found to be $\mu_{electron} = 80.0$ and in a similar fashion the standard deviation σ for the dE/dx electron was found to be $\sigma = 4.5$. For selection of electrons, all electron candidates' measured dE/dx were required to be between -1 to 3σ in agreement with other analyses [4], hence all electrons, for all p_T ranges, were required to be within $75.5 \leq dE/dx \leq 93.5$. Figure 15 shows two transverse momentum bin projections of the dE/dx distributions for electrons with the gaussian fit applied between $dE/dx = 71$ and $dE/dx = 91$.

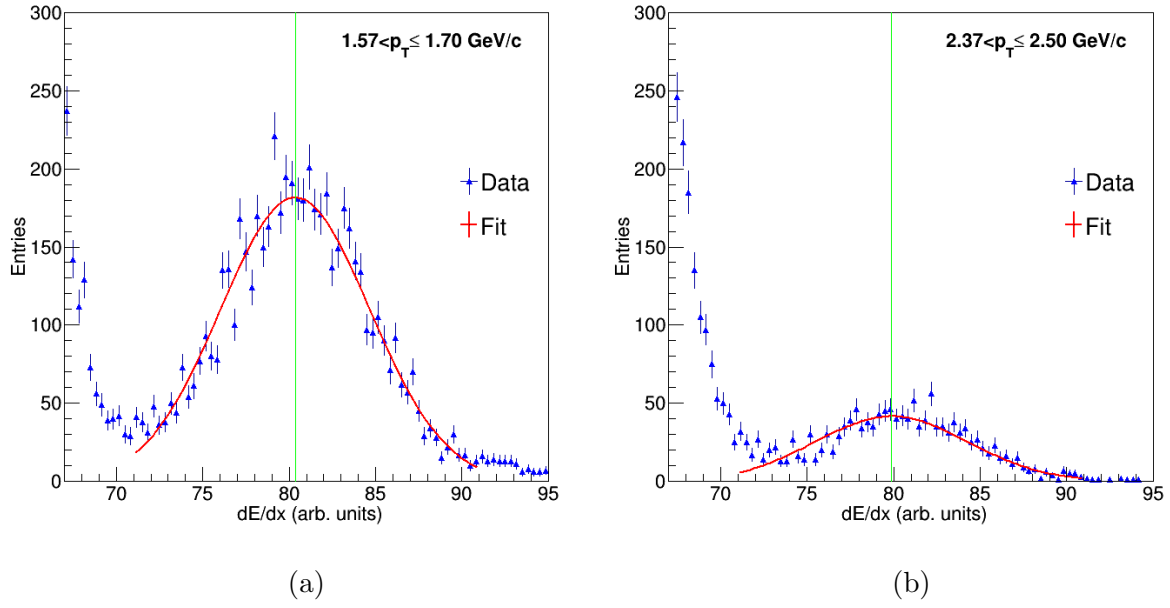


Figure 15: Examples of dE/dx distributions for two different p_T bins (a) at $p_T = 1.63$ GeV/ c with electron dE/dx mean found to be 80.4 with standard deviation 4.3 and (b) at $p_T = 2.43$ GeV/ c with mean electron dE/dx found to be 79.9 with standard deviation 4.8. The green line indicate the mean dE/dx calculated with the fit.

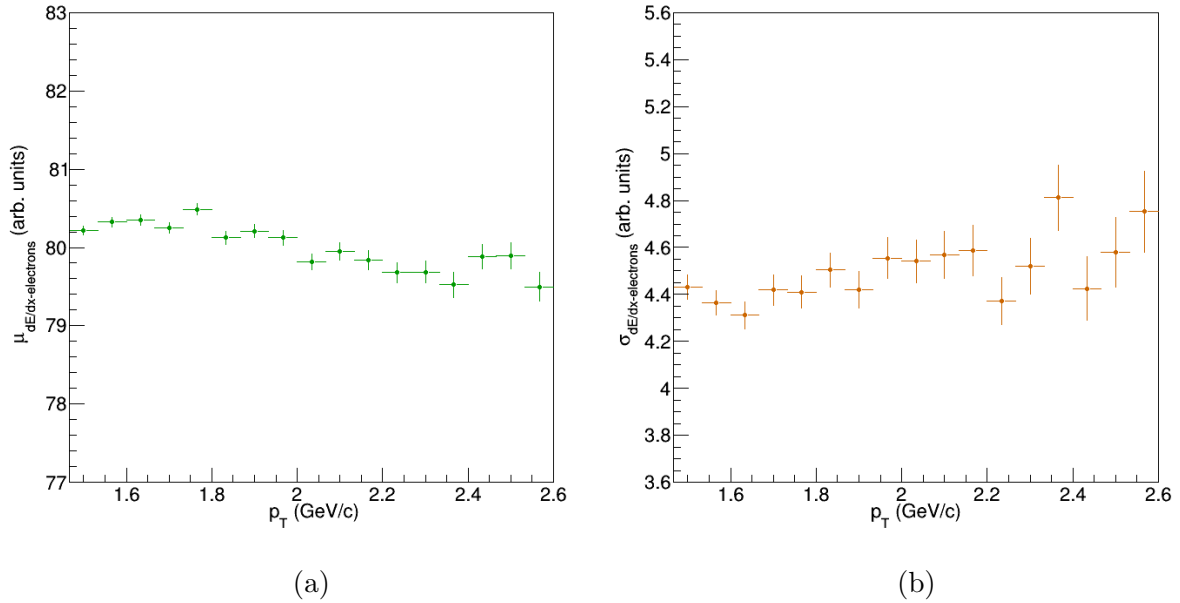


Figure 16: Fit results (a) mean electron dE/dx $\mu_{dE/dx\text{-electrons}}$ as a function of p_T and b) standard deviation $\sigma_{dE/dx\text{-electrons}}$ of $\mu_{dE/dx\text{-electrons}}$ for 17 different p_T bins between 1.5 and 2.6 GeV/ c .

Figure 16 shows the found mean $\mu_{dE/dx\text{-electrons}}$ for each of the 17 p_T bins used to study the dE/dx distribution for electrons and the standard deviation $\sigma_{dE/dx\text{-electrons}}$ of the mean found for each p_T bin.

Non-electron contributions in the electron candidate sample were minimized by cuts on the track energy deposited and momentum measurements, as measured with the EMCal. The shower from an electron is fully measured by the EMCal so that the ratio of the electron energy E , measured by EMCal, and the electron momentum p , (E/p), is approximately unity, whereas the E/p distribution is qualitatively different for hadrons [4]. Therefore electrons were required to be within the range $0.8 < E/p < 1.2$. Since the primary interest here was to study electrons from heavy-flavor hadron decays, electron candidates were required to have a transverse momentum larger than $p_T = 2$ GeV/ c , which also allows for reduction of hadron contamination of the electron candidate sample. Figure 17 shows the ratio E/p as a function of the energy loss dE/dx for $p_T > 2$ GeV/ c in the range $0.2 < E/p < 2$, and $58 < dE/dx < 95$.

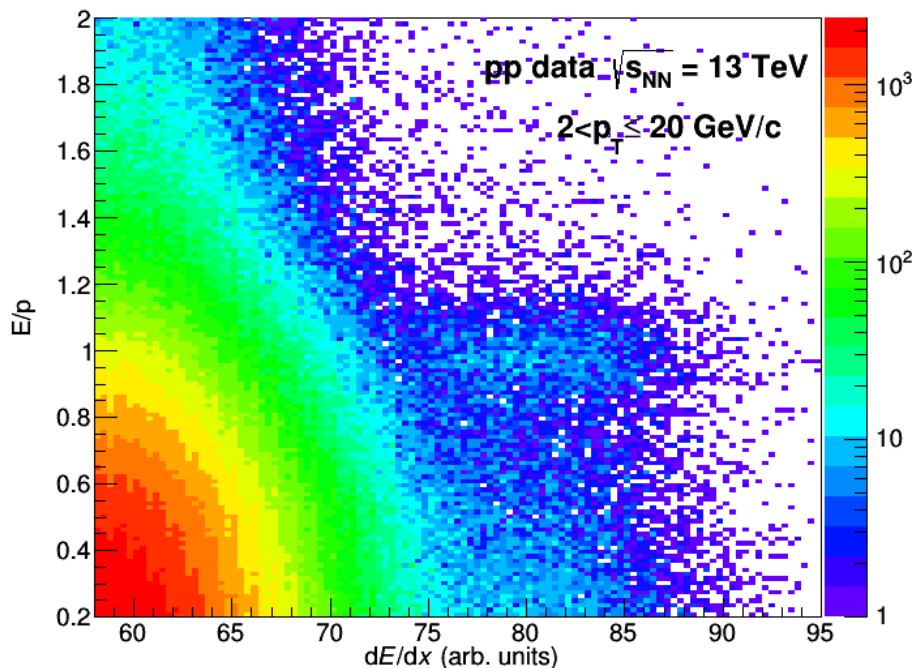


Figure 17: The ratio of E/p as a function of dE/dx at $p_T > 2$ GeV/ c in pp events. p and E are the charged particle momentum and energy measured with EMCal while dE/dx , the ionization energy loss, is measured in the TPC

5.5 Non-electron background subtraction

The non-electron background within the sample of electron candidates, was estimated using the E/p vs. dE/dx distribution shown in Figure 17. The shape of the background in the E/p distribution at the position of the electron peak ($0.8 < E/p < 1.2$ and $75.5 \leq dE/dx \leq 93.5$), was constructed using the track distribution of dE/dx for hadron-dominated tracks, at $dE/dx < 75.5$. To enable subtraction of this background from the electron candidate E/p peak, the hadron background E/p distribution was normalized to match the E/p distribution of the electron candidate away from the true electron peak, at $0.4 < E/p < 0.8$, in agreement with other analyses [4]. Hence, the E/p distributions of the hadrons in $0.4 < E/p < 0.8$ and $0.8 < E/p < 1.2$ are expected to be proportional to each other. The E/p distributions of the non-electron candidates, the estimated background

contamination and the final subtraction of the background from the electron candidates sample are shown for four different p_T intervals in Figure 18.

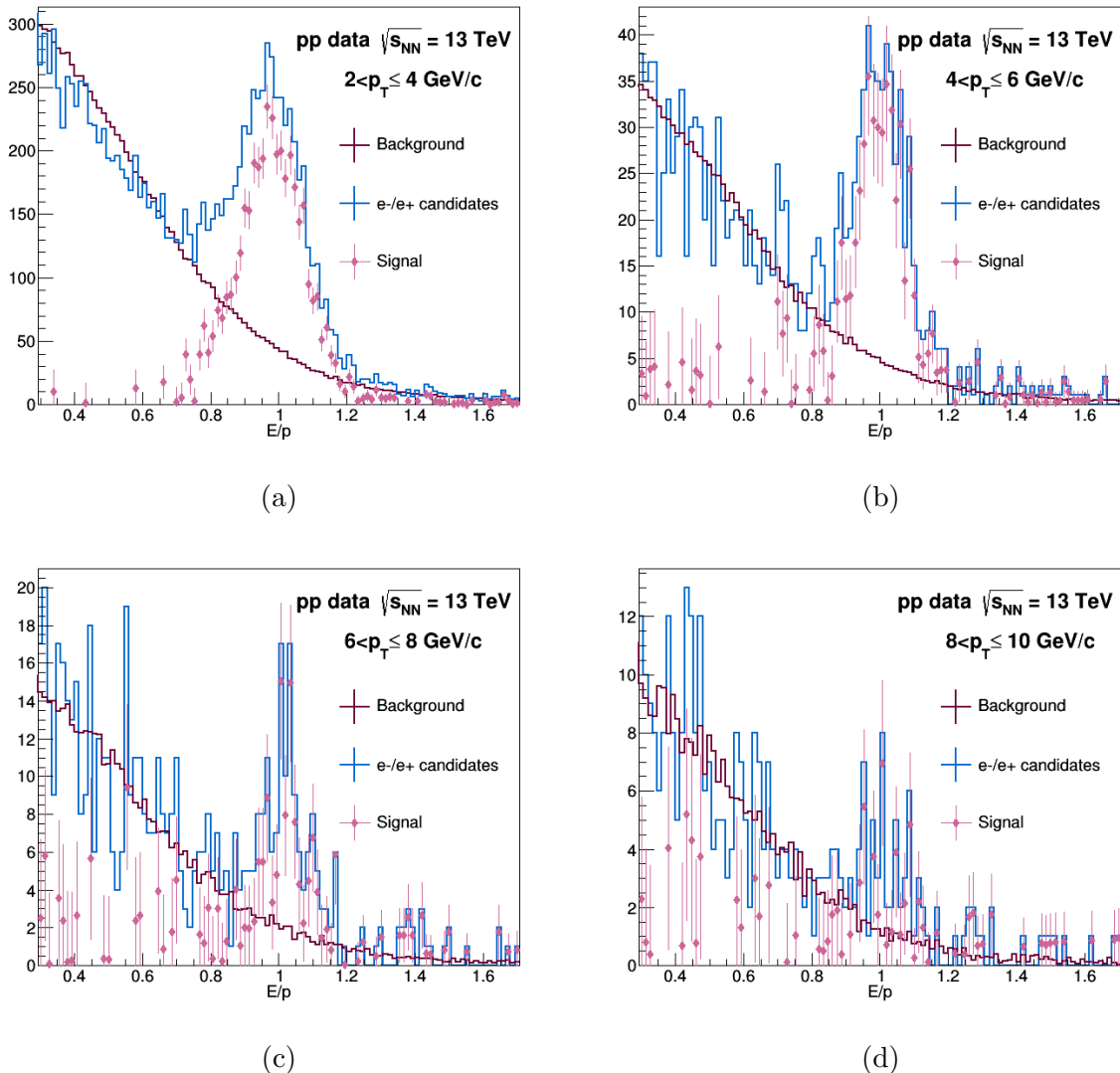


Figure 18: E/p distribution of electron candidates in four transverse momentum ranges. In blue the raw E/p distribution, in red the non-electron background estimation and in pink the raw distribution minus the background distribution, constituting the signal. (a), (b), (c) and (d) show the distributions in $2 < p_T \leq 4$, $4 < p_T \leq 6$, $6 < p_T \leq 8$ and $8 < p_T \leq 10$ GeV/ c , respectively.

From the E/p distributions, as given in Figure 18, the raw electron yield (the number of $e^{+/-}$ candidates), the background and the electron yield minus the hadronic background (signal) was counted as the integral of the distributions in each p_T bin, for the range $2 < p_T < 10$ GeV/ c and separately for $p_T > 10$ GeV/ c . The yields are given in Section 6.

5.6 Photon electron rejection

The sources most interesting to us, of electrons contributing to the electron tracks selected, that should constitute the electron candidate sample, is a composition of electrons from open heavy-flavor hadron decays and electrons from leptonic decays of quarkonia.

Additionally the sample also contains electron candidate contributions from electron decays of $W^{+/-}$ and Z^0 , photonic electrons from photon conversions and Dalitz decays of neutral mesons, dominantly from π^0 and η and kaon decays and contributions from neutral kaon decays to electrons [4].

To exclude the photon conversion electrons in the electron candidate sample, the invariant mass (M_{inv}) of the electron candidate sample was studied. The invariant mass was calculated by pairing of each electron candidate track with an oppositely-charged track. Every electron track candidate, found with track selection and dE/dx -cut as outlined in section 5.4, was paired with an oppositely-charged track, selected with the requirements on DCA_{xy} , DCA_z and η as specified for electrons, but these tracks were not limited by any transverse momentum cut or the electron- E/p -cut. The oppositely-charged tracks were allowed a broader range in specific energy loss such that the track was within 3σ of the mean dE/dx of an electron ($65.6 < dE/dx < 93.5$) to increase the possibility of finding electron pairs.

To exclude electrons originating from photon conversions all tracks giving rise to a pair of $M_{\text{inv}} < 0.1 \text{ GeV}/c^2$ were to be excluded from the electron candidate sample. However, the selected unlike-sign pairs contain not only true pairs of photonic electrons but also a contribution from random pairs making up a combinatorial background. The combinatorial background within the distribution of pairs selected, the background to photon electrons, was estimated by the invariant mass of like-sign electron pairs following the same selection of tracks. Before excluding tracks giving rise to $M_{\text{inv}} < 0.1 \text{ GeV}/c^2$, the invariant mass distributions for unlike-sign pairs and like-sign pairs M_{inv} were studied for MC Rec and data. Further, through use of PDG-identification, the number of tracks originating from heavy-flavor hadrons and photons that would be excluded by a cut $M_{\text{inv}} < 0.1 \text{ GeV}/c$ was estimated. Figure 19 shows the invariant mass distribution of unlike-sign pairs and like-sign pairs for $M_{\text{inv}} \leq 1 \text{ GeV}/c^2$ for (a) MC Rec and (b) data.

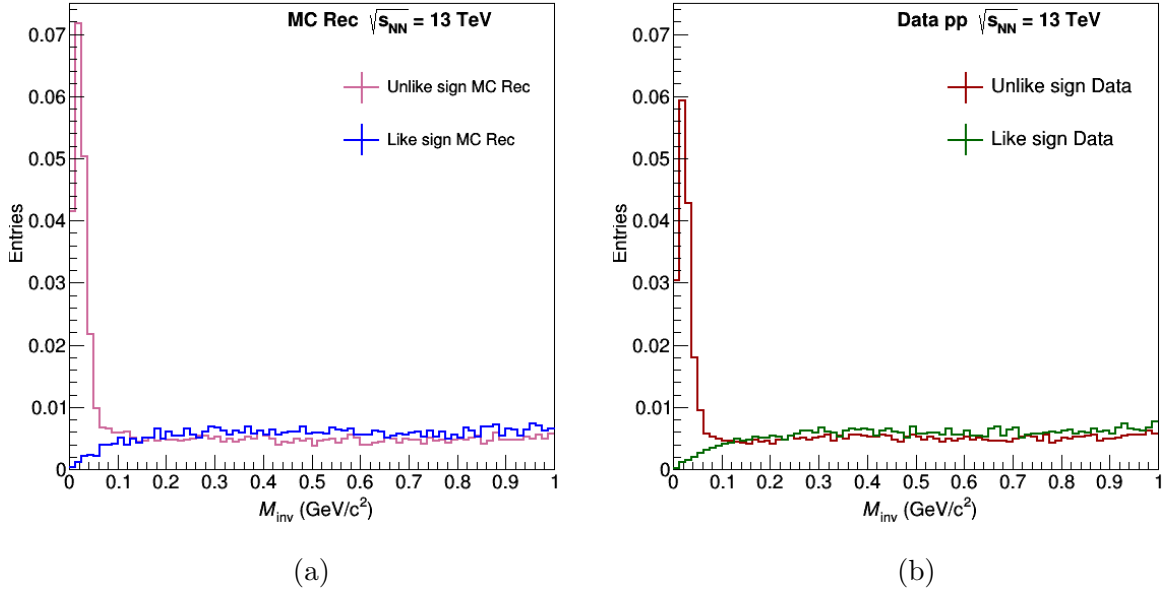


Figure 19: The invariant mass distribution of unlike-sign pairs and like-sign pairs for (a) MC Rec and (b) data, where each electron sample track is matched with every other track within $65.6 < dE/dx < 93.5$, for $M_{\text{inv}} \leq 1 \text{ GeV}/c^2$. The distributions have been normalized to the number of events.

As can be seen in Figure 19, the invariant mass distribution for the unlike-sign pairs show a peak at $M_{\text{inv}} < 0.1 \text{ GeV}/c^2$. Due to the very low invariant mass the track pairs giving rise to $M_{\text{inv}} < 0.1 \text{ GeV}/c^2$ is further excluded in the electron candidate sample.

By study of the electron candidate sample in MC Rec an estimate of the number of eliminated electrons was made. The total number of tracks in the electron candidate sample was calculated for four different groups of mother-types: photons, b-hadrons, c-hadrons and other mothers. This was made possible by the use of identification of the electrons in MC Rec. Further, the total number of true electrons were identified for each mother-type group and subsequently the total number of electron candidates as well as true electrons that were excluded through the rejection of unlike-sign pairs cut on $M_{\text{inv}} < 0.1 \text{ GeV}/c^2$.

Table 3 gives the total number of tracks in the electron candidate sample, as well as how many of them that are true electrons. The table also shows how many of the electron candidates, and of the true electrons, that are excluded from the electron candidate sample by the cut on M_{inv} , for each mother type group respectively. As can be seen in the table, the cut on M_{inv} effectively reduces the number of electrons from photon mothers. Out of the total true electrons from photons, the number is through the invariant mass cut reduced by 0.523. From the electron candidates, out of which not all are true electrons, the number of tracks with photon mothers are reduced by 0.540 through the invariant mass cut.

Table 3: The table lists the number of electron candidates for each mother particle type, how many of them that are rejected through the photon rejection invariant mass analysis and the ratio of electron candidates lost due to the invariant mass cut. Similarly, the table lists the number of true electrons within the electron candidate sample and how many, as well as the fraction, of them that are rejected by the invariant mass cut.

Mother type	Num. of electron candidates	Num. of rejected electron candidates	Ratio	Num. of true electrons (among electron cand.)	Num. of. rejected true electrons	Ratio
All	19281	5246	0.272	8782	2561	0.292
γ	6855	3703	0.540	3490	1824	0.523
b	3268	242	0.0741	1639	113	0.0689
c	5219	145	0.0278	2546	78	0.0306
other	3939	1156	0.293	1107	546	0.4932

As a test of the reliability of the effectiveness of the photon rejection calculated for MC Rec, the invariant mass distributions of unlike-sign pairs and like-sign pairs respectively for MC Rec, were compared to those of data. Figure 20 shows the invariant mass M_{inv} distributions for (a) unlike-and (b) like-sign pairs, for both MC Rec and real data, where the histograms have been normalized to the number of events. Below the ratio of data and MC Rec is shown in each figure. Since the ratio is close to unity for the full M_{inv} range, the ratio of rejected electron candidates and true electrons, as indicated for MC Rec in Table 3, is assumed to be the same for real data.

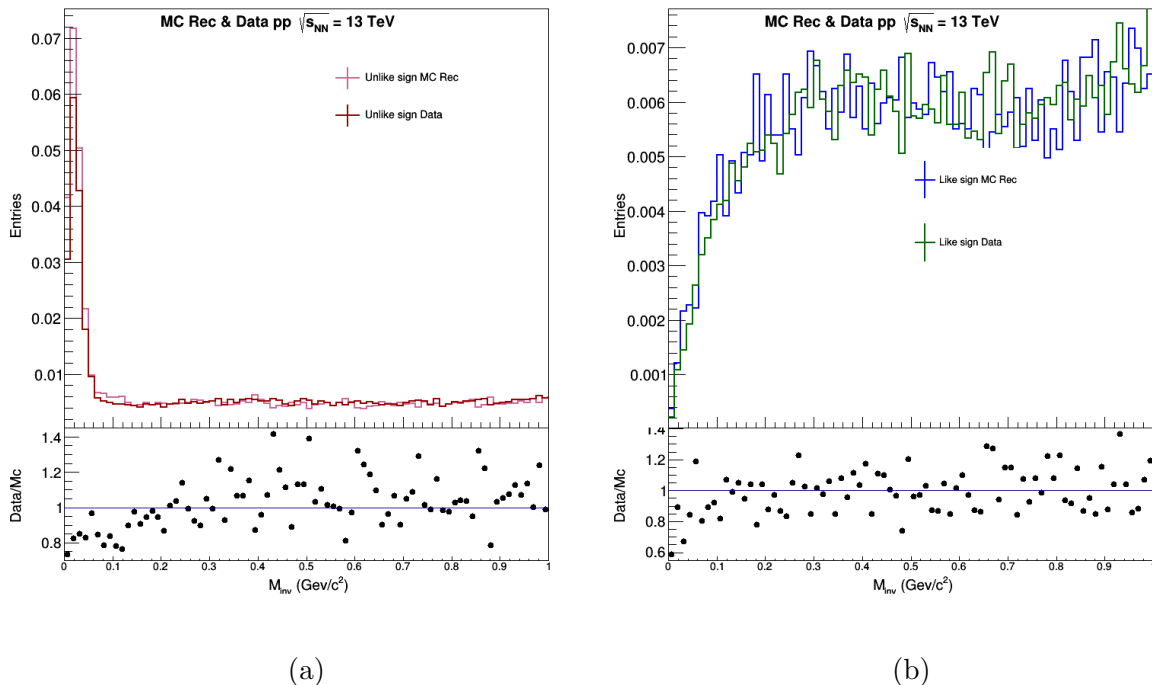


Figure 20: The invariant mass distribution of (a) unlike-sign pairs and (b) like-sign pairs for MC Rec and data. Each electron sample track is matched with every other track within $65.6 < dE/dx < 93.5$, for $M_{\text{inv}} \leq 1 \text{ GeV}/c^2$.

Once the photons had been rejected, the electron yield was again calculated with the non-electron contribution from background as outlined in section 5.5. Figure 21 shows the E/p

distributions for four transverse momentum ranges where the photon rejection has first been made followed by an estimation of the non-electron background. In comparison with Figure 18 one can see that, as expected, the electron yield has gone down with photon rejection applied. From the E/p distributions, as given in Figure 21, the electron yield with photon rejection and the background subtracted was calculated as the integral of the signal distribution for the range $2 < p_T < 10$ GeV/ c and separately for $p_T > 10$ GeV/ c . The yields calculated are given in Section 6.1.

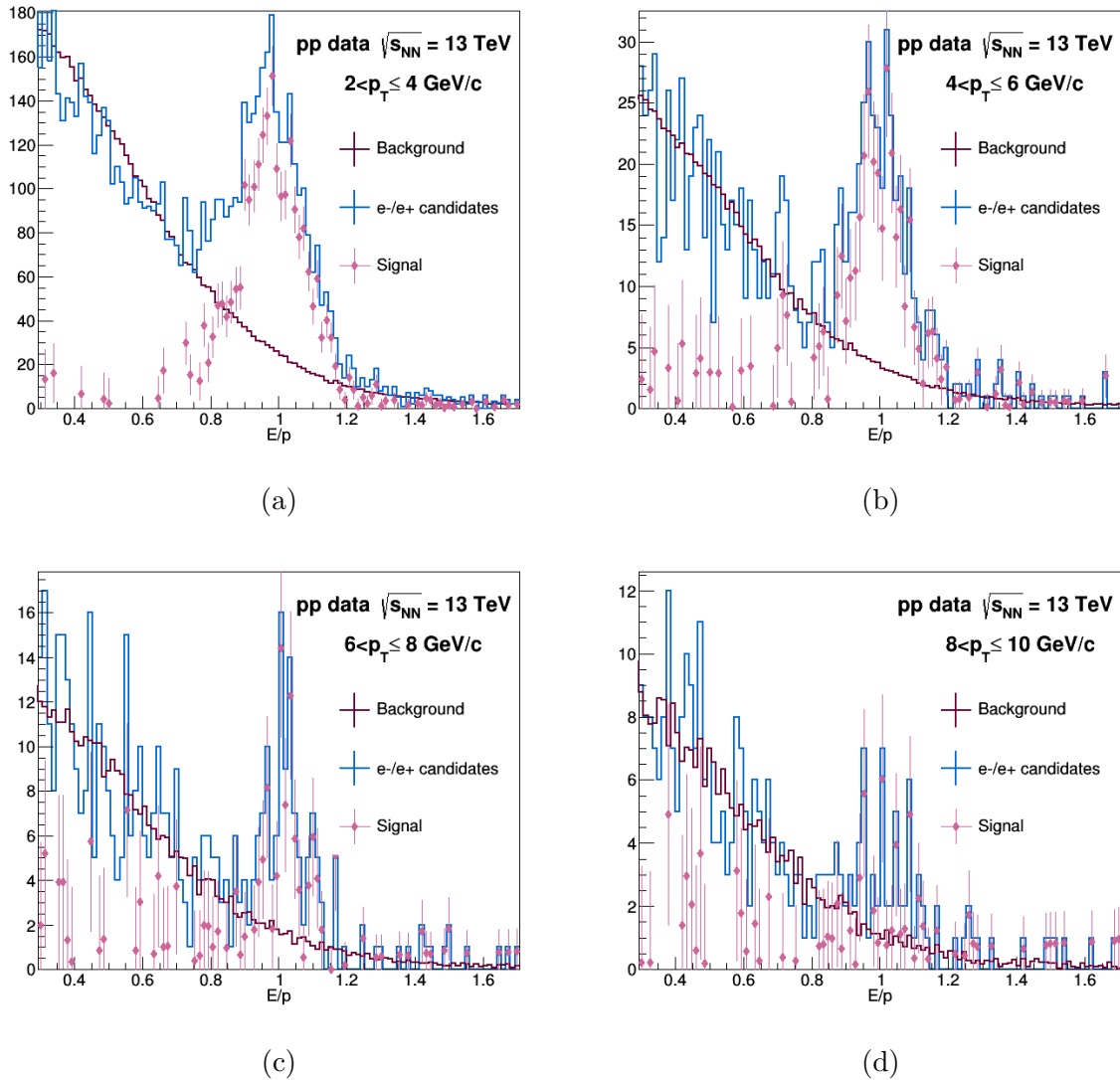


Figure 21: E/p distribution of electron candidates in four transverse momentum ranges where photon rejection has been applied before estimation of the non-electron background. In blue the raw E/p distribution, in red the non-electron background estimation and in pink the raw distribution minus the background distribution, constituting the signal. (a), (b), (c) and (d) show the distributions in $2 < p_T \leq 4$, $4 < p_T \leq 6$, $6 < p_T \leq 8$ and $8 < p_T \leq 10$ GeV/ c , respectively.

5.7 Detector efficiency

The ratio between the amount of reconstructed and detected particles and the total number of generated particles in a collision is the detector efficiency. The efficiency is due

to a detector's inability to detect and record all particles created in a collision and is calculated using MC simulations. The efficiency of the heavy-flavor electron production is the number of MC Rec electron candidates divided by the number of electrons in MC Gen. Figure 22 shows the simulated detector efficiency for four different cases of electron candidates: (1) with track selection and the electron dE/dx -cut (in green), (2) with track selection, electron- dE/dx -cut and photon rejection (in pink), (3) with track selection, electron- dE/dx -cut and electron- E/p -cut and (4) with full electron PID. In Figure 22, the electron candidates have been identified using the particle identification only, whereas in 22 (b), the PDG-markers have been used to identify true electrons. The cuts referred to here are exactly the ones described in Section 5.4. It is observed that the value of the efficiency quantity, shown in Figure 22 (a), reaches values above unity at higher p_T indicating contamination in the electron candidate sample.

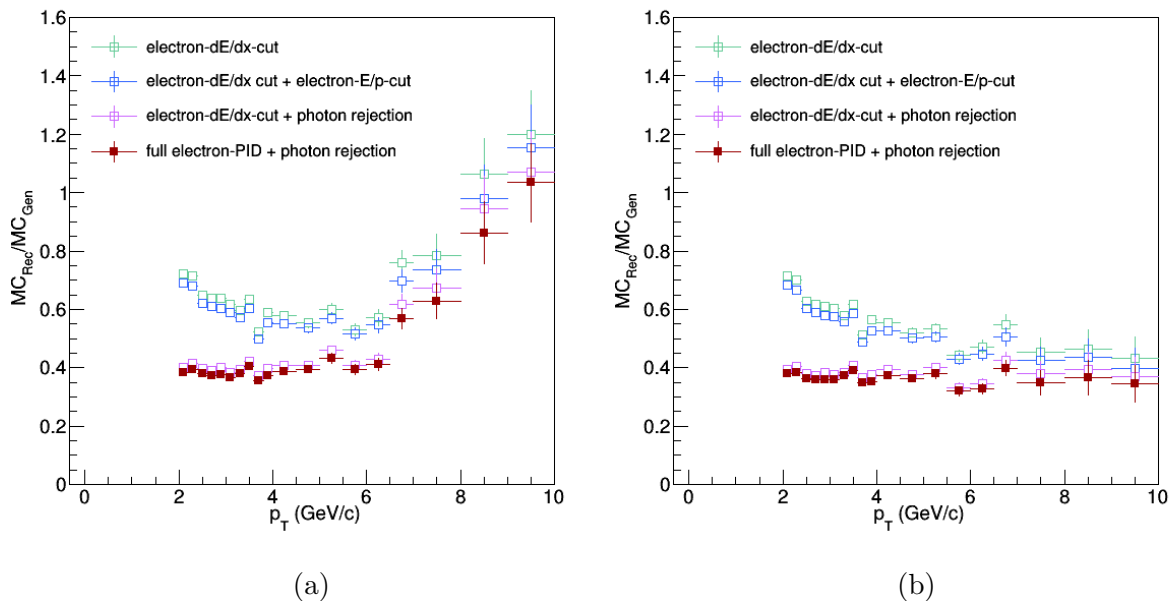


Figure 22: Simulated detector electron identification efficiency distributions where (a) all reconstructed tracks have gone through track selection and then additional electron dE/dx cut (in light blue), electron dE/dx -cut and photon rejection (in blue), electron dE/dx -cut and electron E/p -cut (in pink) and all electron PID (in red) and (b) where all reconstructed MC electrons have been identified in the same fashion as in (a) but where the electrons are required to be true electrons as identified with PDG markers.

Figure 22 (a) shows that the photon rejection and full electron PID effectively reduces the number of electron candidates at $2 < p_T < 6$ GeV/c, where the efficiency shown in red is fairly stable at around 0.4. At higher p_T , ($p_T > 6$ GeV/c) there are contributions to the electron candidates that are less successfully removed by the PID and the photon rejection. Figure 22 (b), where the reconstructed electron candidates are required to be true electrons, show that the efficiency is stable around 0.4 for the full p_T -range here studied.

Before applying the simulated detector efficiency to the real data electron yields, data electron p_T distributions were compared to those of MC Rec, for the different electron candidate cuts and the final electron PID. Below, Figure 23 shows the p_T distributions

of tracks passing track selection and (a) electron dE/dx -cut, (b) electron dE/dx -cut and photon rejection, (c) electron dE/dx -cut and electron E/p -cut and (d) all tracks passing the full electron PID, for MC Rec and data. The data and MC Rec distributions are normalized to the number of events in the data and the MC Rec, respectively. Below each p_T distribution the ratio between the two distributions are displayed. As can be seen, up to about $p_T = 5 - 6$ GeV/ c , all the distribution ratios are approximately unity, whereas for higher p_T the ratios are above 1. As an example, Figure 23(a) indicates that contamination of the electron sample becomes important at $p_T = 6$ GeV/ c . Most importantly, it can be seen in Figure 23(d) that the ratio is approximately unity up to ≈ 8 GeV/ c , and for higher p_T -ranges the statistics are very low. Subsequently, the detector efficiency calculated for the full PID, as shown in 22 (a) was used to compensate for the detector deficiency in the calculated heavy-flavor yields, shown in Section 6.1.

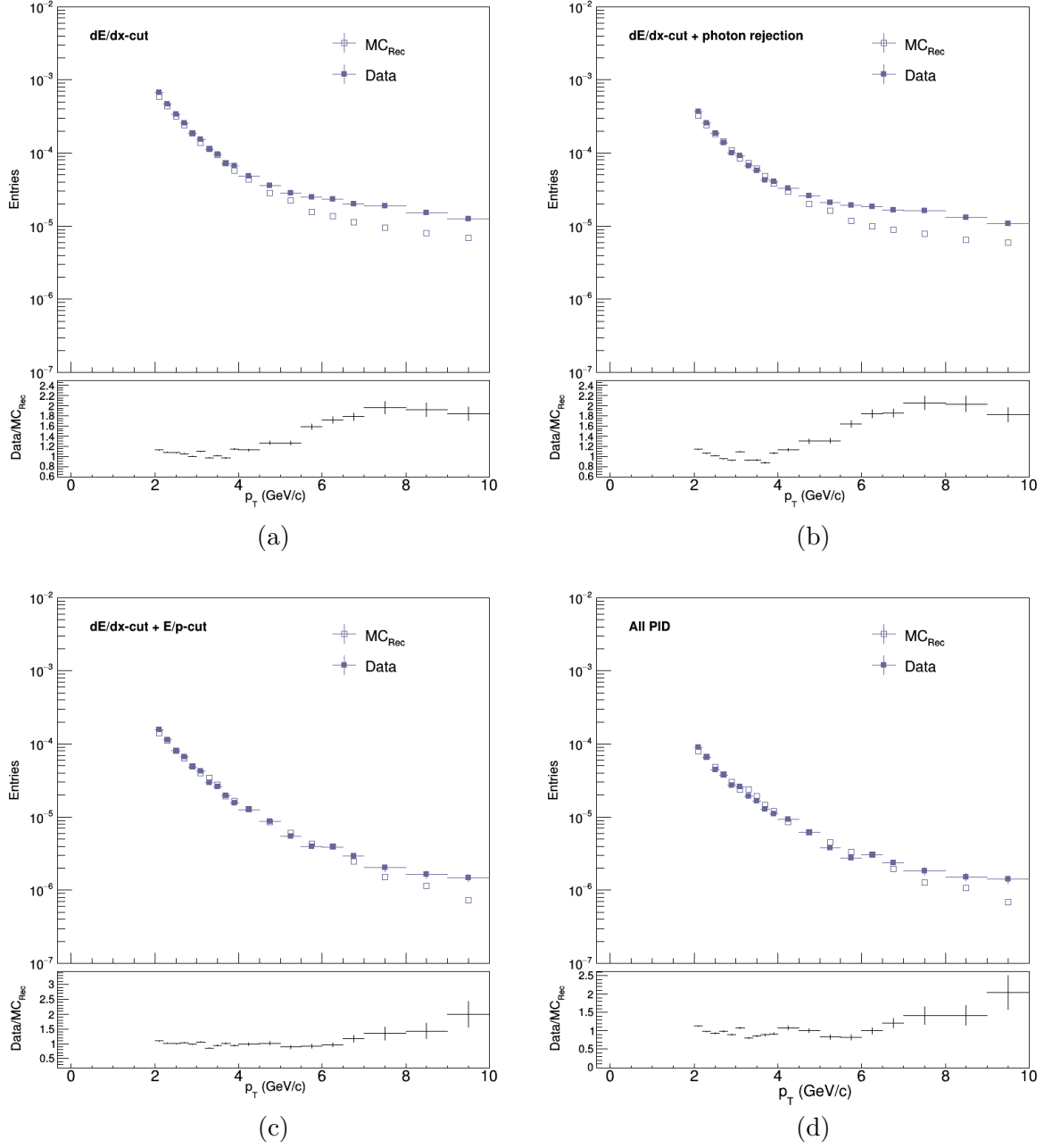


Figure 23: p_T distributions for tracks passing track selection and (a) the electron dE/dx -cut, (b) the electron dE/dx -cut and photon rejection, (c) electron dE/dx -cut and electron E/p -cut and (d) with the full electron PID, for MC Rec and data. Below each figure the ratio between the data and the MC Rec is displayed. As seen, the p_T distribution ratios are close to unity for low p_T ($p_T < 5 - 6\text{GeV}/c$), whereas the ratio goes up for higher p_T .

5.8 Electron mother DCA distribution analysis

Due to bottom and charm hadrons long life times, ($c\tau \approx 500 \mu\text{m}$ for bottom hadrons and $c\tau \approx 100 - 300 \mu\text{m}$ for $D^{+/0}$ charm hadrons (which are the abundant charm-source of electrons), see Table 2) these hadrons decay at a secondary vertex, displaced from the primary collision vertex. Thus, electron tracks from semileptonic heavy-flavor hadron decays have a broad distance of closest approach (DCA) distribution, as compared to those from lighter quark hadrons [6]. The DCA is a measurement of the distance between the reconstructed track and the primary vertex and is divided into two components: DCA_{xy} is the distance of closest approach in the plane transverse to the beam direction and DCA_z is the distance of closest approach along the beam direction.

With the aim to distinguish heavy-flavor hadron contributions from other sources of electrons the DCA_{xy} distribution has been studied for the three different groups of electron mothers discussed before: b-hadron mother electrons, c-hadron mother electrons and other mother electrons (where the other mother group contains the same mother-particles as described in Section 5.2). All identified electrons, the sum of the three groups, were defined as the True electrons in MC Rec.

Firstly, all electron source groups were identified in MC Rec, with the available PDG identification for both particle and its mother-particle. By study of the DCA distributions of the three mother groups, and the sum of them defined as all True electrons, a fractional yield, the *Generated fractional yield*, of each type of electron mother was found. The fractional yields are for each and every mother group defined as the number of b-,c- or other-mother electrons (N_{e_b} , N_{e_c} and N_{e_o}), as given by the DCA_{xy} distribution, divided by the total number of electrons, for the distribution. Hence, the fractional yields are given by

$$\frac{N_{e_b}}{N_{e_b} + N_{e_c} + N_{e_o}}, \quad \frac{N_{e_c}}{N_{e_b} + N_{e_c} + N_{e_o}} \quad \text{and} \quad \frac{N_{e_o}}{N_{e_b} + N_{e_c} + N_{e_o}},$$

for b-mother electrons, c-mother electrons and other-mother electrons respectively.

A fraction fit was performed using the three mother groups as templates by fitting the three mother group DCA_{xy} distributions to the DCA_{xy} distribution of the True electrons. To perform the fit, all mother group DCA distributions were normalized to the True electron DCA_{xy} distribution. The fraction fit function was constructed by adding together the contributions from the three mother groups then trying to fit the function to the True electron distribution by a χ^2 minimization. From the fraction fit the *Measured fractional yields* were extracted.

Figure 24 shows a first example of the DCA distributions for $2 < p_T \leq 3 \text{ GeV}/c$ and Figure 25 a second example of the same distributions for $4 < p_T \leq 5 \text{ GeV}/c$. The figures 24 and 25 show (a) the initial DCA_{xy} distributions for the three mother groups and the True electrons, from which the generated fraction yields for each mother group are extracted and (b) the DCA_{xy} distributions of the three mother groups and the True electrons, where the mother group distributions have been normalized to the True electron DCA distributions and the fraction fit has been applied, generating the measured fractional fit.

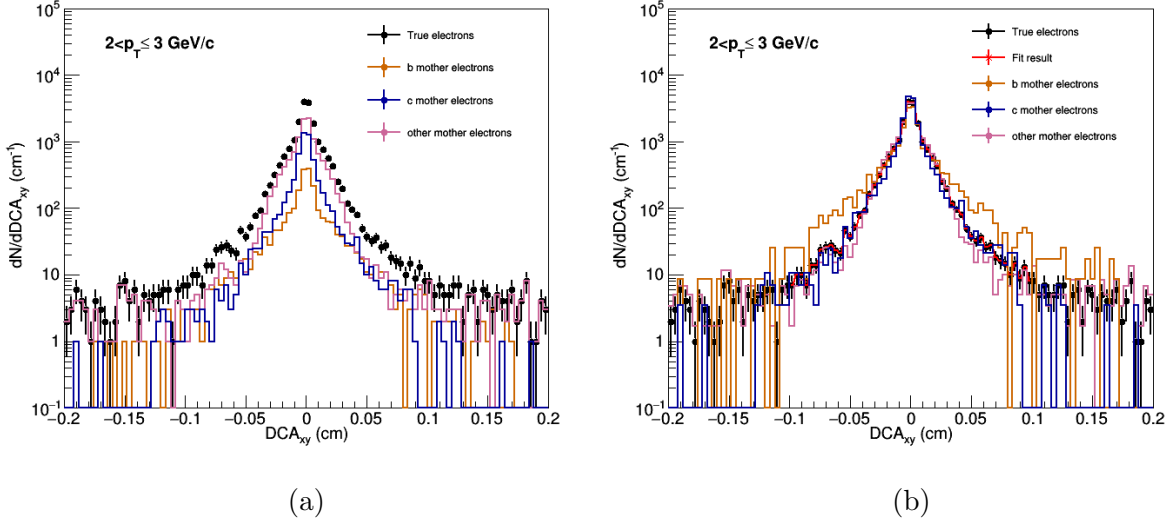


Figure 24: Electron DCA_{xy} distributions of reconstructed MC in the range $2 < p_T \leq 3 \text{ GeV}/c$. The True electron distribution is shown in black, the b-mother electron distribution in orange, the c-mother electron distribution in blue and the other-mother electron distribution in pink. (a) shows the distributions without fitting, (b) the distributions where the three mother groups have been normalized to the True electron distributions as input to the fraction fit, and the fraction fit result indicated.

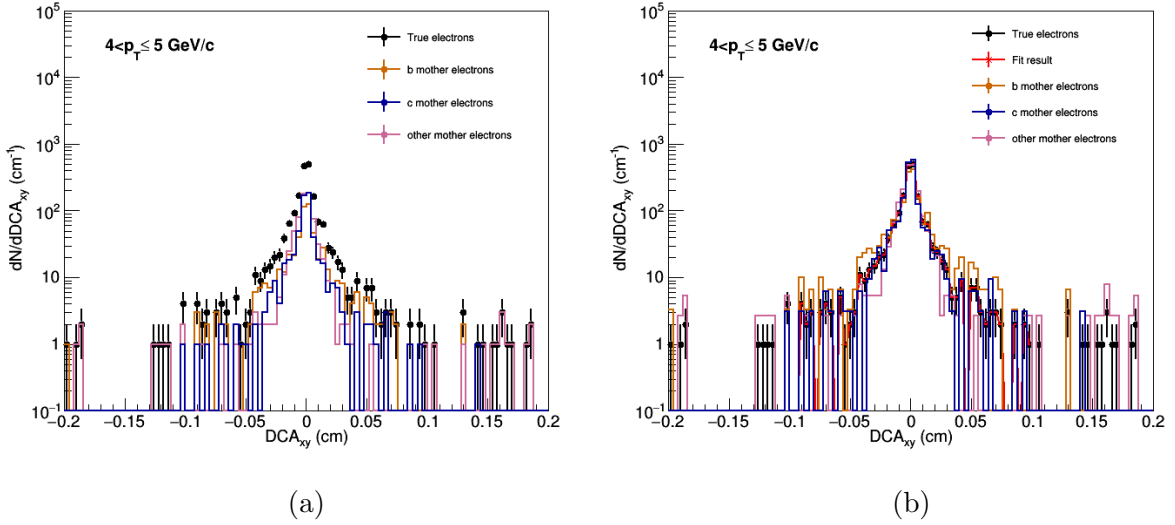


Figure 25: Electron DCA_{xy} distributions of reconstructed MC in the range $4 < p_T \leq 5 \text{ GeV}/c$. The True electron distribution is shown in black, the b-mother electron distribution in orange, the c-mother electron distribution in blue and the other-mother electron distribution in pink. (a) shows the distributions without fitting and (b) the distributions where the three mother groups have been normalized to the True electron distributions as input to the fit and the fit result.

Note that the tails of the c-mother distributions (blue) is broader for higher p_T as compared to the lower p_T range, as seen by comparing 25 (b) with 24 (b).

Using the three different mother groups as outlined above, the DCA_{xy} distributions were also found for identified electrons in the analyzed data. The same analysis, finally extracting the measured fractional yields, was made for data by replacing the True electron DCA distributions with that of electron candidates. The electron candidates were selected as outlined in Section 5.4 and photon rejection was performed as described in Section 5.6. The DCA_{xy} distributions for the electron data candidates have been normalized to the True electron DCA_{xy} distributions, to be able to study the difference in the shape of the distributions.

The figures below show (a) the initial DCA_{xy} distributions for the three mother groups and the electron candidates, from which the generated fraction yields for each mother group are extracted, and (b) the DCA distributions of the three mother groups and the electron candidates, where the mother group distributions have been normalized to the electron candidate DCA_{xy} distributions, and the fraction fit has been applied, generating the measured fractional fit.

Figure 26 and Figure 27 show the DCA distributions for $2 < p_T \leq 3 \text{ GeV}/c$ and $4 < p_T \leq 5 \text{ GeV}/c$ for electrons identified in data. The figures show (a) the initial DCA_{xy} and the electron candidates in data and (b) the DCA_{xy} distributions of the three mother groups and the electron candidates.

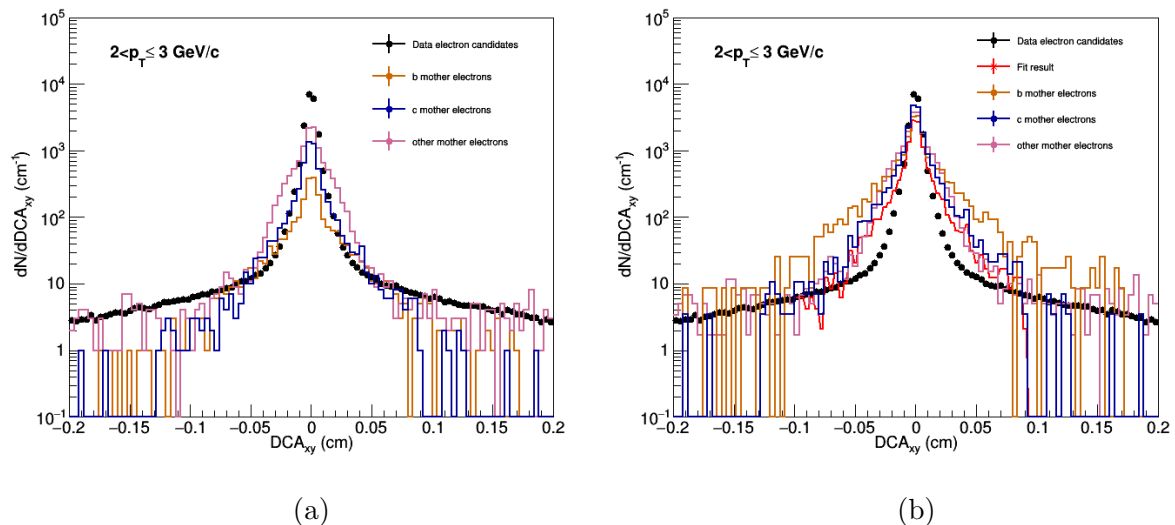


Figure 26: Electron DCA_{xy} distributions of data for the range $2 < p_T \leq 3 \text{ GeV}/c$. The data electron distribution is shown in black, the b-mother electron distribution in orange, the c-mother electron distribution in blue and the other-mother electron distribution in pink. (a) shows the distributions without fitting and (b) the distributions where the three mother groups have been normalized to the True electron distributions and with the fit applied.

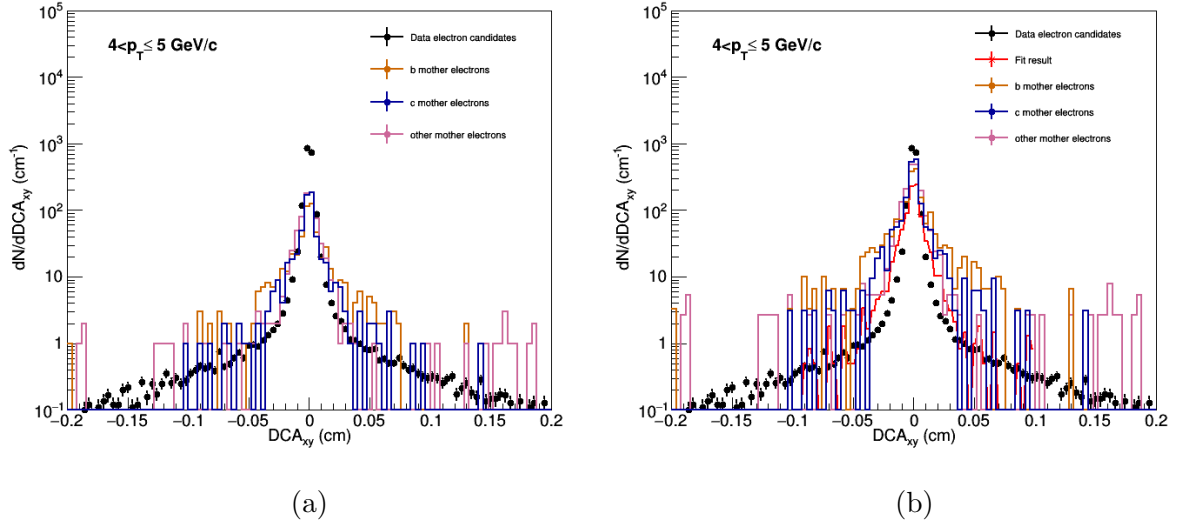


Figure 27: Electron DCA_{xy} distributions of data for the range $4 < p_T \leq 5 \text{ GeV}/c$. The data electron distribution is shown in black, the b-mother electron distribution in orange, the c-mother electron distribution in blue and the other-mother electron distribution in pink. (a) shows the distributions without fitting and (b) the distributions where the three mother groups have been normalized to the True electron distributions and with the fit applied.

Figure 26 and 27 show that the distributions of data electron candidates have a much narrower peak, as compared to that of MC Rec True electrons. Due to the broader distributions of all the electron mother group distributions, the fraction fit fails to fit the shape of the mother group distributions to that of the electron candidates shape. This is especially visible for the b-mother distribution as the measured fraction yield goes to zero for all p_T ranges where the DCA_{xy} distributions were studied. This gave the result that not all measured fractional yields added up to unity, as should be the case.

6 Results and discussion

6.1 Electron yield from spectra analysis

Figure 28 and Figure 29 show the heavy-flavor electron raw yield, the electron raw yield with background subtraction and the background without and with photon rejection applied, respectively. The yields have been corrected for the efficiency found, as discussed in Section 5.7 and the rapidity window ($|y| < 0.6$). As earlier seen in Section 5.6, the electron yield due to photons is effectively reduced by the photon rejection. The uncertainties indicated in the yields are calculated Poisson distribution errors. The yields shown in Figure 28 and Figure 29 are of electrons from both b- and c- quarks and cover the range $p_T > 5$ GeV/c where the production of electrons is dominated by heavy-flavor semileptonic decays. However, the electrons from b- and c- quark hadrons are in this analysis not disentangled from each other.

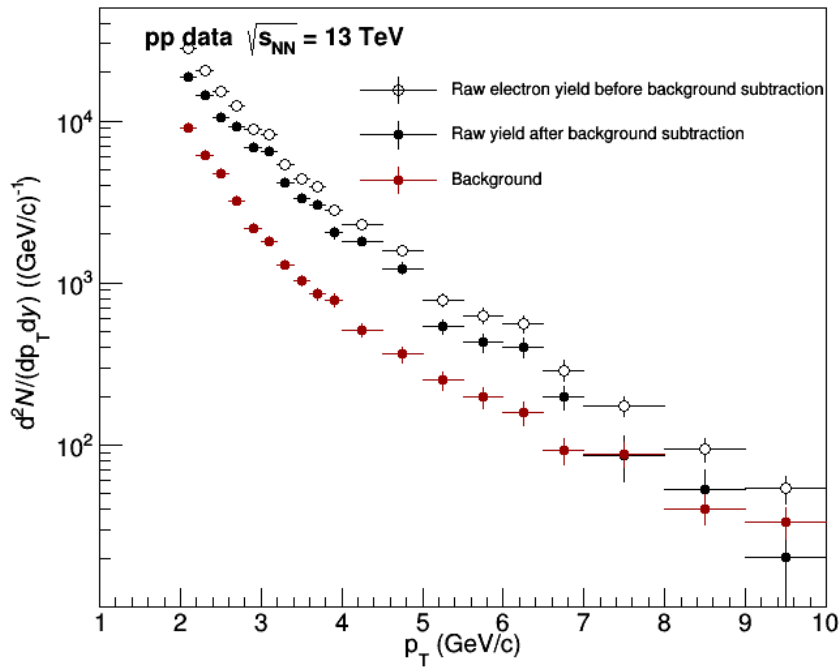


Figure 28: Heavy-flavor electron yield for the range $2 < p_T < 10$ GeV/c.

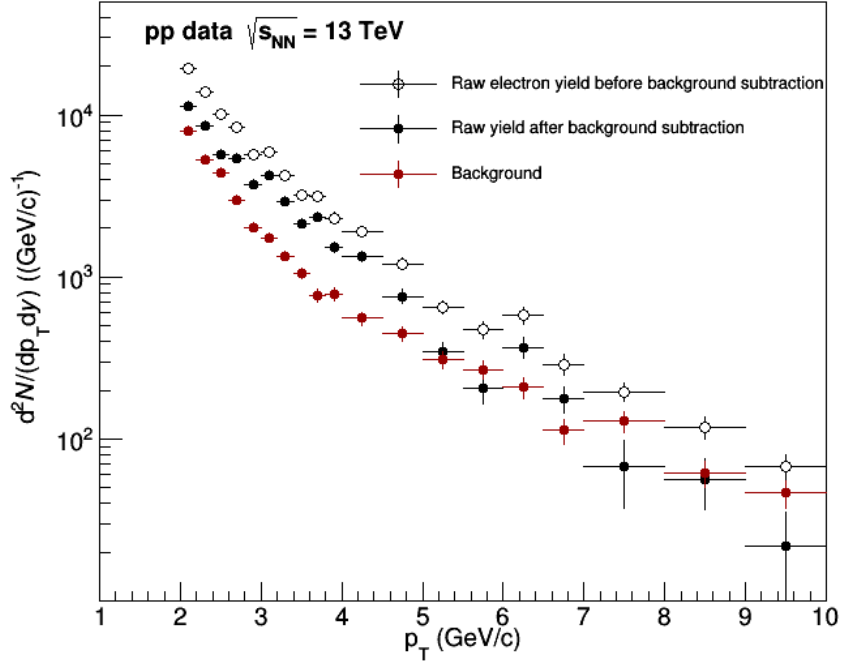


Figure 29: Heavy-flavor electron yield with applied photon rejection for the range $2 < p_T < 10$ GeV/ c .

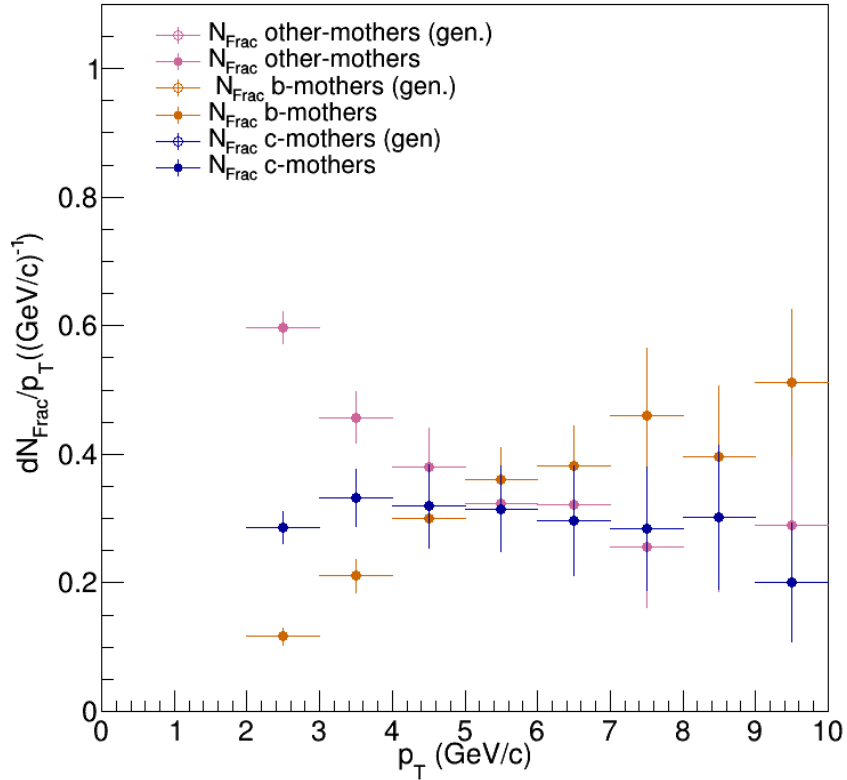
Table 4 lists the raw electron yield, the raw electron yield with background subtraction and its uncertainty without and with photon rejection.

Table 4: Electron yield with background subtraction and electron yield with photon and non-electron background subtraction

p_T -range (GeV/ c)	Raw yield	Yield w. bkgd subtraction	Uncertainty	Raw yield w. photon rejection	Yield w. photon rejection and bkgd subtraction	Uncertainty
2.0-2.2	19328.8	13086.2	± 375.2	13480.4	7915.4	± 220.5
2.2-2.4	14276.9	10051.6	± 330.2	9658.3	5988.4	± 190.0
2.4-2.6	10601.3	7308.0	± 281.4	7010.8	3976.1	± 151.5
2.6-2.8	8615.0	6404.8	± 74.0	5835.4	3750.2	± 154.4
2.8-3.0	6227.0	4732.7	± 229.2	3962.7	2564.0	± 120.3
3.0-3.2	5719.5	4476.9	± 245.0	4119.3	2914.6	$\pm 151.$
3.2-3.4	3761.1	2868.7	± 174.7	2950.8	2018.9	± 114.7
3.4-3.6	3054.2	2330.2	± 154.2	2217.4	1486.8	± 93.2
3.6-3.8	2714.3	2122.5	± 157.3	2171.4	1636.4	± 111.0
3.8-4.0	1965.1	1418.0	± 119.9	1607.8	1062.4	± 83.5
4.0-4.5	1603.8	1247.8	± 88.6	1322.5	936.6	± 69.8
4.5-5.0	1104.8	852.7	± 74.6	837.9	528.0	± 53.8
5.0-5.5	547.6	373.5	± 41.0	454.6	240.0	± 34.0
5.5-6.0	436.1	298.3	± 38.8	329.9	143.2	± 29.6
6.0-6.5	389.8	279.4	± 39.0	400.7	256.0	± 37.2
6.5-7.0	201.2	136.8	± 23.0	201.2	122.9	± 22.0
7.0-8.0	121.5	60.1	± 11.9	136.2	46.7	± 20.8
8.0-9.0	65.4	37.2	± 8.1	82.0	39.0	± 13.4
9.0-10.0	37.4	14.1	± 4.3	47.3	15.0	± 9.6

6.2 DCA_{xy} distribution fractional yields

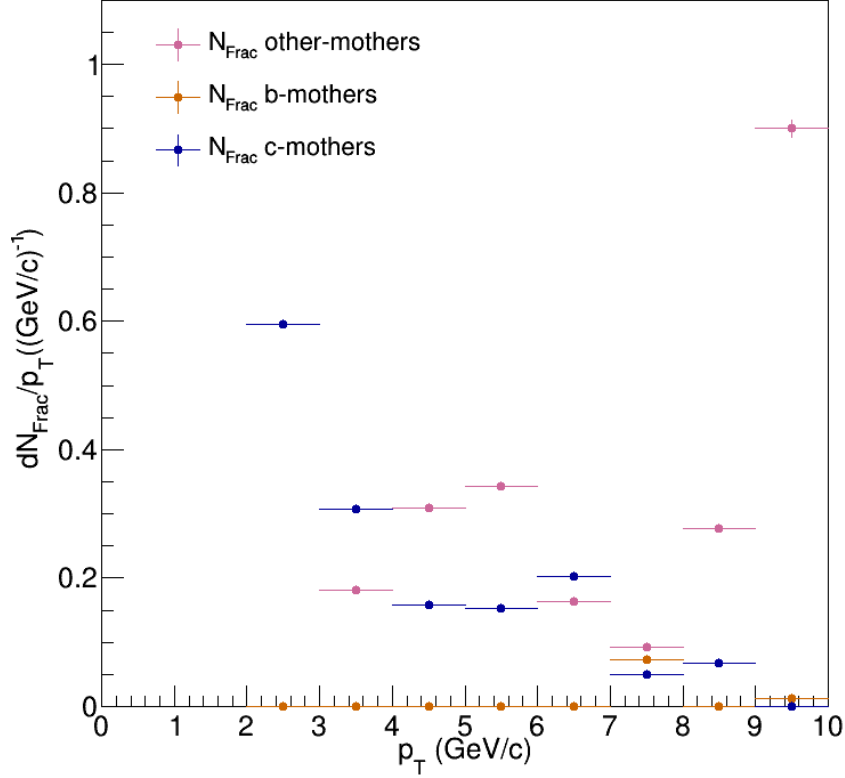
Figure 30 shows the generated and measured fractional yields as a function of p_T for MC Rec. As indicated in the figure, the electron yield due to other mother decays dominates at $p_T < 5$ GeV/c, whereas the heavy-flavor electron production dominates at higher p_T ranges.



(a) MC

Figure 30: Fractional yield for MC Rec. The measured and generated fractional yield are so close in value that the generated fractional yields are not visible.

Figure 31 shows the measured fractional yields as a function of p_T for MC Rec. Here, the fractional yield of electrons due to b-hadron decays are for almost all p_T ranges zero, which we know should not be the case. Also, the fractional yields measured for other-mothers and c-hadron mothers do not correspond to the expected results as given by 30.



(b) Data

Figure 31: Fractional yield for data. It's visible that the fraction fit fails to reproduce the b-hadron contribution to the electron candidate sample.

Tables 5 and 6 list the fractional yields for MC Rec and data, respectively, with the uncertainties indicated. As can be seen in Table 5, the generated and measured fractional yields for all mother groups correspond well with each other. In Table 6 one can see that the fraction fit applied to the DCA_{xy} distributions failed to reproduce the contribution from b-mother electrons. Where no numbers are given, the fractional yield was either zero or below 10^{-10} .

Table 5: Measured and generated fractional yields for MC Rec

p_T (GeV/c)	Gen. $N_{\text{frac-b}}$	Meas. $N_{\text{frac-b}}$ (\pm uncertainty)	Gen. $N_{\text{frac-c}}$	Meas. $N_{\text{frac-c}}$ (\pm uncertainty)	Gen. $N_{\text{frac-o}}$	Meas. $N_{\text{frac-o}}$ (\pm uncertainty)
2.0-3.0	0.118	0.117 ± 0.013	0.286	0.286 ± 0.024	0.597	0.597 ± 0.024
3.0-4.0	0.211	0.211 ± 0.025	0.332	0.332 ± 0.0410	0.457	0.457 ± 0.037
4.0-5.0	0.300	0.300 ± 0.041	0.320	0.320 ± 0.061	0.380	0.380 ± 0.055
5.0-6.0	0.362	0.362 ± 0.049	0.315	0.315 ± 0.066	0.323	0.323 ± 0.059
6.0-7.0	0.383	0.383 ± 0.060	0.296	0.296 ± 0.0789	0.321	0.321 ± 0.071
7.0-8.0	0.460	0.460 ± 0.103	0.285	0.285 ± 0.091	0.255	0.255 ± 0.092
8.0-9.0	0.400	0.400 ± 0.110	0.302	0.302 ± 0.112	0.302	0.302 ± 0.116
9.0-10.0	0.511	0.511 ± 0.112	0.200	0.200 ± 0.091	0.289	0.289 ± 0.100

Table 6: Measured fractional yields for data

p_T (GeV/c)	Meas. $N_{\text{frac-b}}$ (\pm uncertainty)	Meas. $N_{\text{frac-c}}$ (\pm uncertainty)	Meas. $N_{\text{frac-o}}$ (\pm uncertainty)
2.0-3.0	-	0.595 ± 0.004	-
3.0-4.0	-	0.308 ± 0.002	0.181 ± 0.002
4.0-5.0	-	0.158 ± 0.002	0.310 ± 0.003
5.0-6.0	-	0.152 ± 0.003	0.342 ± 0.003
6.0-7.0	-	0.203 ± 0.003	0.164 ± 0.003
7.0-8.0	0.073 ± 0.003	0.050 ± 0.002	0.092 ± 0.003
8.0-9.0	-	0.068 ± 0.003	0.278 ± 0.006
9.0-10.0	0.012 ± 0.002	0.001 ± 0.002	0.900 ± 0.013

6.3 Conclusion and outlook

In conclusion, Figures 18 and 21 show that the method for non-electron background subtraction works well, for $p_T < 8 \text{ GeV}/c$, as seen in 18 (a), (b) and (c), but is not as successful for higher p_T ($p_T > 8 \text{ GeV}/c$), as seen in Figure 18 and Figure 21 (d). As seen in Figure 13, the heavy-flavor contribution to the electron candidates dominate at $p_T > 5 \text{ GeV}/c$. Hence, many of the electrons identified in the sample for $p_T < 5 \text{ GeV}/c$ are due to mother particles of other types. However, as seen in Figure 28 and Figure 29, the electron yields are given for p_T ranges ($p_T > 5 \text{ GeV}/c$), where the electron production is dominated by heavy-flavor semileptonic decays.

Photon contributions are well reduced by the photon rejection performed, as explained in Section 5.6. Due to low statistics, the analysis was not possible for higher p_T intervals than $p_T = 10 \text{ GeV}/c$. This could be resolved by having more events to study. However, it should be noted that the EMCal electron identification dominantly reduces the statistics to a great extent.

The background considered and finally subtracted from the raw yield of heavy-flavor electrons is a composition of different hadrons, such as pions that should contribute to the dE/dx spectrum considered, especially for low p_T . To avoid contamination from other electrons, only photons were rejected from the electron candidates. Rejection of electrons from $W^{+/-}$ and Z^0 decays could also have been made, although this contribution should be small. Due to lower statistics at the highest p_T ranges considered for the electron, the spread in the yield goes up for high p_T .

From studies of the efficiency for the different electron-PID-cuts and full electron PID, as seen in Figure 22 for both MC Rec with electrons identified as in data in (a) and (b) true electrons, it can be seen that the efficiency is largely affected by the electron EMCal (E/p -cut)-identification and the photon-electron rejection. Up to about $p_T = 6 \text{ GeV}/c$ the electron particle identification in data is well described by the same efficiency calculated for true electrons. For higher p_T ($p_T > 6 \text{ GeV}/c$) the data electron candidates are contaminated, as can be seen by comparing 22 (a) and (b). The difference indicates that the signal to background ratio is lowered for higher p_T which probably is caused by lower statistics, i.e. a lower number of events available, for the higher p_T ranges.

To distinguish between sources of electrons (heavy-flavor b and c mothers, and other mothers) the DCA_{xy} distributions were studied and fitted using a χ^2 -fit. As can be seen in the MC Rec DCA_{xy} distributions in Figure 24 and 25, and finally in the distribution of the N_{frac} in 30 (a), the fractional fit reproduces the DCA_{xy} distributions described by MC Rec well. The fractional yields obtained for the data electron DCA_{xy} distributions, shown in Figure 30 (b) did however not correspond to the fractional yields obtained in MC Rec. This is due to fail of the fitting of the different shapes of the DCA_{xy} distributions of data electrons as compared to that of true electrons identified in MC Rec.

The difference in the shapes of the DCA_{xy} distributions, comparing data and MC Rec distributions, shows that the resolution is better in the data sample as compared to that of MC Rec. If more time was available for the analysis, the fractional fit would be reviewed further and evaluated again with the data possibly re-scaled. The fail in the fit indicates that the χ^2 -fit overshoots when trying to fit the two distributions together and

minimizing the difference between the two.

The DCA_{xy} fraction fit method worked well for MC, as it should since all the information available should be consistent. The method could however have been checked better with independent statistics samples. Since the data distributions are narrower than any, and all, MC DCA_{xy} distributions there is simply no way to have a successful outcome for fits to data for this data analysis.

A natural continuation of the outlined analysis would involve trying to disentangle the electron yield contributions from b- and c-quarks respectively by use of the different shapes of the p_T distributions of electrons from b- and c-hadrons as seen in Figure 12. However, as seen in the DCA_{xy} analysis presented here, it should be noted that the difference in shape of the MC Rec electrons as compared to data identified electrons could cause the same kind of problems as encountered for the disentanglement mentioned.

References

- [1] ALICE INFO;. <http://aliceinfo.cern.ch/Public/Welcome.html>.
- [2] Info A;. http://aliceinfo.cern.ch/Public/en/Chapter2/Chap2_TPC.html.
- [3] Cortese P, et al. ALICE electromagnetic calorimeter technical design report. 2008;.
- [4] Adam J, et al. Measurement of the production of high- p_T electrons from heavy-flavour hadron decays in Pb-Pb collisions at $\sqrt{s_{NN}} = 2.76$ TeV. Phys Lett. 2017;B771:467–481.
- [5] Abelev BB, et al. Measurement of electrons from semileptonic heavy-flavor hadron decays in pp collisions at $\sqrt{s} = 2.76$ TeV. Phys Rev. 2015;D91(1):012001.
- [6] Abelev B, et al. Measurement of electrons from beauty hadron decays in pp collisions at $\sqrt{s} = 7$ TeV. Phys Lett. 2013;B721:13–23. [Erratum: Phys. Lett.B763,507(2016)].
- [7] <http://www.physics.umd.edu>; Last visited on 16 November 2017.
- [8] WikiMedia. Standar Model;. https://commons.wikimedia.org/wiki/Standard_Model.
- [9] Thomson M. Modern Particle Physics; 2013.
- [10] Kane G. Modern Elementary Particle Physics; 1993.
- [11] Cronodon P. QCD;. <http://cronodon.com/Atomic/QCD.html>.
- [12] Averbek R. Heavy-flavor production in heavy-ion collisions and implications for the properties of hot QCD matter. Prog Part Nucl Phys. 2013;70:159–209.
- [13] Nayak T. Search for the QCD Critical Point at RHIC: First Experience with Au-Au Collisions at 9.2 GeV;. <https://www.bnl.gov/rhic/news/040808/story3.asp>.
- [14] Shaw M. Particle Physics; 1993.
- [15] ALICE Servotech;. https://alice-servotech.web.cern.ch/ALICE-ServoTech/HELP_D/CDB-SVT/HelpFiles/ALICE-INT-2003-038.pdf.
- [16] Florowski W. Phenomenology of Ultra-Relativistic Heavy-Ion Collisions; 2010.
- [17] Cern Courier;. www.cerncourier.com.
- [18] Iancu E. QCD in heavy ion collisions. In: Proceedings, 2011 European School of High-Energy Physics (ESHEP 2011): Cheile Gradistei, Romania, September 7-20, 2011; 2014. p. 197–266. Available from: <https://inspirehep.net/record/1113441/files/arXiv:1205.0579.pdf>.
- [19] Matsui T, Satz H. J/ψ Suppression by Quark-Gluon Plasma Formation. Phys Lett. 1986;B178:416–422.
- [20] Abreu MC, et al. The Dependence of the anomalous J/ψ suppression on the number of participant nucleons. Phys Lett. 2001;B521:195–203.

- [21] Andronic A, Braun-Munzinger P, Redlich K, Stachel J. Statistical hadronization of heavy quarks in ultra-relativistic nucleus-nucleus collisions. Nucl Phys. 2007;A789:334–356.
- [22] Abelev B, et al. J/ψ suppression at forward rapidity in Pb-Pb collisions at $\sqrt{s_{NN}} = 2.76$ TeV. Phys Rev Lett. 2012;109:072301.
- [23] Collider LTLH. <http://home.cern/topics/large-hadron-collider>; Last visited on 16 November 2017.
- [24] The ATLAS experiment;. <https://atlas.cern/discover/about>.
- [25] The CMS experiment;. <https://home.cern/about/experiments/cms>.
- [26] The LHCb experiment;. <http://lhcb-public.web.cern.ch/lhcb-public/>.
- [27] LHC. LHC outreach;. <https://lhc-machine-outreach.web.cern.ch/lhc-machine-outreach/>.
- [28] ALICE. aliceinfo;. <http://aliceinfo.cern.ch/Public/en/Chapter2/Chap2InsideAlice-en.html>.
- [29] Bryngemark L. Charged pion identification at high pT in ALICE using TPC dE/dx. In: 6th International Workshop on High-pT physics at LHC (HPT 2011) Utrecht, The Netherlands, April 4-7, 2011; 2011. Available from: <https://inspirehep.net/record/927004/files/arXiv:1109.1896.pdf>.
- [30] Diaries Q. EMCAL;. <http://www.quantumdiaries.org/2010/10/13/meet-the-alice-electromagnetic-calorimeter/>.
- [31] Brun R, Rademakers F. ROOT: An object oriented data analysis framework. Nucl Instrum Meth. 1997;A389:81–86.
- [32] Sjostrand. Pythia;. <http://home.thep.lu.se/torbjorn/Pythia.html>.
- [33] Geant;. <http://geant.cern.ch/>.
- [34] Particle Data Group (PDG);. <http://pdg.lbl.gov/>.

7 Appendix

All DCA_{xy} distributions MC Rec:

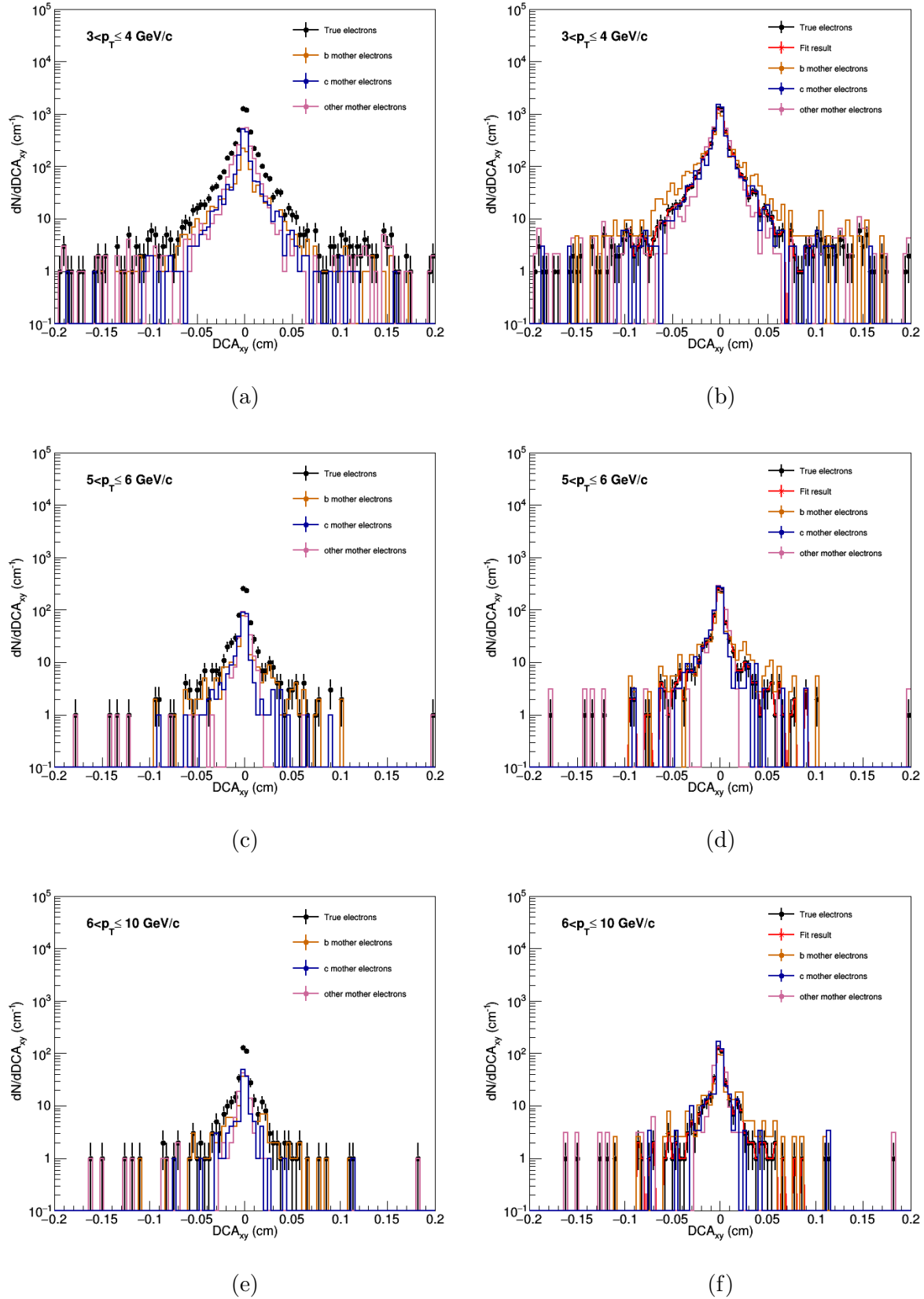


Figure 32: MC Rec DCA_{xy} distributions.

All DCA_{xy} distributions data:

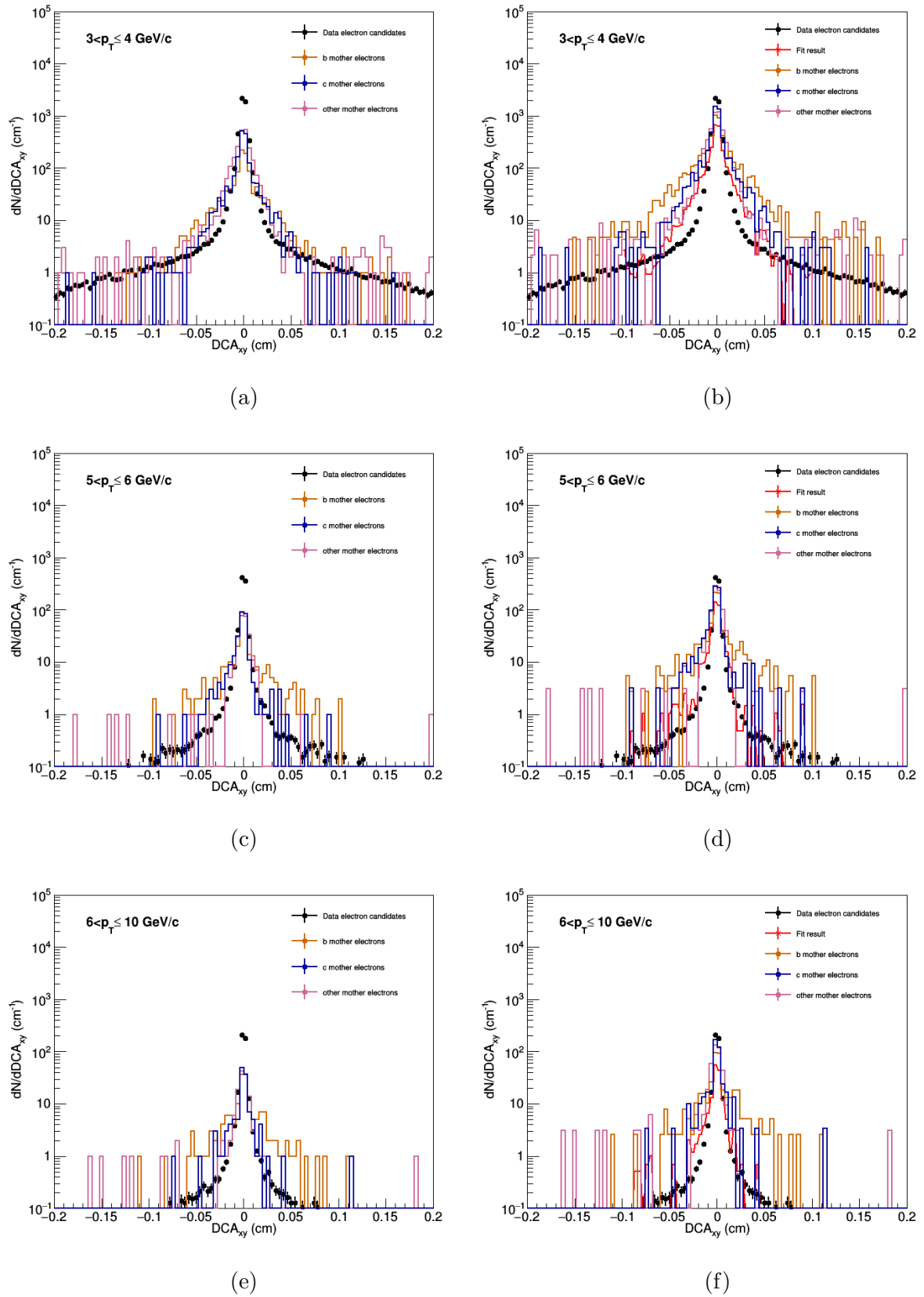


Figure 33: Data DCA_{xy} distributions.